

# Superdeformation and clustering in $^{40}\text{Ca}$ studied with Antisymmetrized Molecular Dynamics

Y. Kanada-En'yo and M. Kimura

*Yukawa Institute for Theoretical Physics, Kyoto University,  
Kyoto 606-8502, Japan*

Deformed states in  $^{40}\text{Ca}$  are investigated with a method of antisymmetrized molecular dynamics. Above the spherical ground state, rotational bands arise from a normal deformation and a superdeformation as well as an oblate deformation. The calculated energy spectra and  $E2$  transition strengths in the superdeformed band reasonably agree to the experimental data of the superdeformed band starting from the  $0_3^+$  state at 5.213 MeV. By the analysis of single-particle orbits, it is found that the superdeformed state has particle-hole nature of an  $8p$ - $8h$  configuration. One of new findings is parity asymmetric structure with  $^{12}\text{C}$ + $^{28}\text{Si}$ -like clustering in the superdeformed band. We predict that  $^{12}\text{C}$ + $^{28}\text{Si}$  molecular bands may be built above the superdeformed band due to the excitation of inter-cluster motion. They are considered to be higher nodal states of the superdeformed state. We also suggest negative-parity bands caused by the parity asymmetric deformation.

## I. INTRODUCTION

In the spectra of  $^{40}\text{Ca}$ , the existence of low-lying deformed states has long been known since 1960s [1]. The coexistence of the spherical and various deformed states in the doubly magic nuclei  $^{40}\text{Ca}$  has attracted a great interest. In the positive parity states below 7 MeV, besides the spherical ground state, the existence of two deformed rotational bands built on the  $0_2^+$  state at 3.35 MeV and the  $0_3^+$  state at 5.21 MeV is known experimentally. The structure of these bands has been often discussed in relation to many-particle many-hole states of nuclei in this mass region for a long time. Grace and Green [2,3] firstly suggested that the former band is dominantly a  $4p$ - $4h$  state, while the latter band with a large deformation is understood as an  $8p$ - $8h$  state.

The member states of the first  $K^\pi=0^+$  rotational band built on the  $0_2^+$  state are known to be strongly populated by  $\alpha$ -transfer reactions and to have the large  $\alpha$  spectroscopic factors [4–7]. The  $\alpha$ + $^{36}\text{Ar}$  cluster structure of this band has been studied theoretically based on semi-microscopic cluster model calculations [8–10].

The states in the second  $K^\pi=0^+$  band have been observed in the experimental work searching for the  $8p$ - $8h$  states with  $^{32}\text{S}(\text{C},\alpha)^{40}\text{Ca}$  reactions, which were performed by Middleton *et al.* in 1972 [11]. Due to the strong population in the multi-nucleon transfer data and the strong  $E2$  transitions [1], the  $0^+$ (5.21 MeV),  $2^+$ (5.63 MeV) and  $4^+$  (6.54 MeV) have been thought to belong to the superdeformed band with a dominant  $8p$ - $8h$  configuration. Recently, by using the GAMMASPHEAR array detectors, the level structure of the deformed bands in  $^{40}\text{Ca}$  has been explored and many excited states up to very high spins have been discovered [12,13]. Consequently, the existence of the superdeformed band of  $^{40}\text{Ca}$  built on the  $0_3^+$ (5.21 MeV) has been experimentally well established.

In contrast to the experimental situation, theoretical interpretation of the superdeformed band is not well established and is still complicated. With the symmetry restricted Skyrme-Hartree-Fock(HF) calculations, Zheng *et al.* studied the energy systematics of  $n$  particle- $n$  hole( $np$ - $nh$ ) states in  $^{40}\text{Ca}$  [14,15]. They suggested an  $8p$ - $8h$  deformed states as a local minimum of the energy as a function of  $n$ . They also predicted highly deformed  $12p$ - $12h$  states in a high excitation energy region. However, the recent mean-field calculations suggest that the  $8p$ - $8h$  configuration becomes unstable, especially when the model space is extended. Based on the three-dimensional(3d) HF calculations without any assumption of the spatial symmetry, Inakura *et al.* studied the energy surface of  $^{40}\text{Ca}$  as the function of the quadrupole deformation. They have shown that the local minimum of the superdeformed  $8p$ - $8h$  configuration on the energy curve becomes quite shallow or even disappear due to the  $\gamma$  and octupole deformations depending on the effective interaction, though the  $12p$ - $12h$  state and an oblate state remain to be local minima in any of used effective interactions. They have pointed out that the extreme softness of the superdeformed  $8p$ - $8h$  configuration against the octupole deformation ( $Y_{30}$  and  $Y_{31}$ ). The instability of the  $8p$ - $8h$  configuration and the stability of the  $12p$ - $12h$  and oblate solutions in  $^{40}\text{Ca}$  had been also reported by Leander and Larsson [17] based on the macroscopic-microscopic model calculations. Further calculations beyond mean-field theory were performed by Bender *et al.* with GCM calculations in HF+BCS approach [18]. In their results, the superdeformed band is not dominated by a certain  $np$ - $nh$  configuration but it contains various configurations such as  $4p$ - $4h$ ,  $6p$ - $6h$ , and  $8p$ - $8h$  states due to the strong mixture between these configurations. Moreover, shell model calculations were performed for description of the superdeformed bands [19]. Although the level structure and quadrupole moments of the superdeformed band are described by the spherical shell model with the fixed  $8p$ - $8h$  configurations, however, when the model space is extended to include other particle-hole configurations, the quadrupole moments are much underestimated due to the configuration mixing.

These facts may imply that a stable solution for the intrinsic state of the superdeformation is hardly obtained in the modern calculations with mean-field approaches. It seems to be somehow inconsistent with the experimental energy spectra of the superdeformation in which no large deviation from the rigid rotor model is seen [12,13]. Therefore, it is natural to expect that there might be some mechanism beyond mean-field approaches to stabilize the superdeformation. The cluster aspect is one of the essential features for nuclear deformation even in *sd-pf* shell nuclei together with the mean-field aspect. Indeed, it has been already shown that two kinds of nature, i.e. cluster and mean-field coexist in the deformed states in *sd*-shell nuclei [20–22]. We expect that the clustering can play an important role also in the formation of the superdeformed state of  $^{40}\text{Ca}$ . In case of  $^{40}\text{Ca}$ , we consider that the softness against octupole deformations in the superdeformed state suggested by Inakura *et al.* can be associated with asymmetric di-cluster structure, though, to our knowledge, there has been no studies to investigate its cluster aspect.

We also note that some *sd*-shell nuclei have the remarkable cluster aspect, molecular resonances, whose properties have been investigated by cluster models. Recently, there are theoretical efforts to link the molecular resonances with low-lying deformed states with full microscopic calculations. It is suggested that the molecular resonances and the low-lying deformed states in *sd*-shell are regarded to be a series of molecular bands. For example, in  $^{32}\text{S}$  system, it has been suggested that  $^{16}\text{O}$ - $^{16}\text{O}$  molecular resonances are built on the superdeformed band of  $^{32}\text{S}$  [22] owing to the excitation of the inter-cluster motion. Therefore, we consider that molecular resonances can be good probes to understand the cluster aspect of the low-lying deformed states. In  $^{40}\text{Ca}$  system, there are experimental implications of  $^{28}\text{Si}$ + $^{12}\text{C}$  molecular resonances in the low-energy fusion cross section [23] and also elastic scattering data [24], where distinct structures have been found in the energy region  $E_{\text{cm}}=20\text{--}30$  MeV above the  $^{28}\text{Si}$ + $^{12}\text{C}$  threshold. It is interesting to look into possible appearance of molecular resonances and its relation to the superdeformation in  $^{40}\text{Ca}$ .

In this paper, we study deformed states in  $^{40}\text{Ca}$  with antisymmetrized molecular dynamics(AMD). The method of AMD has been proved to be useful in description of shape coexistence as well as cluster structure in *sd*-shell nuclei [20–22,25–29]. One of advantages of this method is that both cluster aspect and mean-field aspect can be described within the AMD framework. In order to study the coexistence of deformations in  $^{40}\text{Ca}$  and to investigate the corresponding rotational bands, we apply a constraint AMD method. Parity projection, which is essentially important to describe the parity asymmetric shape of nuclei, is performed before energy variation, while total-angular-momentum projection is done after the energy variation. We also perform superposition of the wave functions with different configurations obtained by the constraint AMD to obtain better wave functions and to describe possible configuration mixing. Level scheme and  $E2$  transition strengths are calculated from these superposed wave functions. In the present work, we adopt the effective nuclear interaction which contains finite-range 2-body and 3-body forces proposed in Ref. [30]. This interaction is suitable for describing the nuclear structure properties such as binding energies and radii over a wide mass number region from  $^4\text{He}$  to  $^{40}\text{Ca}$ . Moreover, it is also useful to describe nucleus-nucleus potential. These features can not be described by zero-range forces such as the Skyrme forces, and are superior points of the effective forces with finite-range three-body terms. We believe that they are essential to represent cluster aspect and to investigate properties of many-particle-many-hole states with large deformations.

This paper is organized as follows. In section II, the formulation of AMD is briefly explained. In Sec.III, we show the calculated results of the energies, quadrupole transitions and moments, and also the intrinsic structure. We give discussions of molecular aspect and single-particle orbits in Sec.IV. Finally, a summary is given in Sec.V.

## II. FORMULATION

We here briefly explain the formulation of the present calculations. For the details of the AMD formulation for nuclear structure studies, the readers are referred to Refs. [20,31,32].

### A. Intrinsic wave function

We start from the intrinsic wave function for a  $A$ -nucleon system which is expressed by a Slater determinant of single-particle wave packets,

$$|\Phi_{\text{AMD}}\rangle = \frac{1}{\sqrt{A!}} \mathcal{A}\{\varphi_1, \varphi_2, \dots, \varphi_A\}, \quad (1)$$

$$\varphi_i(\mathbf{r}_j) = \phi_i(\mathbf{r}_j) \chi_i \eta_i, \quad (2)$$

where  $\mathcal{A}$  is the antisymmetrizer, and  $\varphi_i$  is the  $i$ th single-particle wave packet consisting of the spatial part  $\phi_i$ , the spin part  $\chi_i$  and the isospin part  $\eta_i$ . The spatial part of the  $i$ th single-particle wave packet is written by a Gaussian wave packet located at  $\mathbf{X}_i$ .

$$\phi_i(\mathbf{r}_j) = \exp\{-\nu(\mathbf{r}_j - \mathbf{X}_i)^2\}, \quad (3)$$

$$\chi_i = (\frac{1}{2} + \xi_i)\chi_{\uparrow} + (\frac{1}{2} - \xi_i)\chi_{\downarrow}, \quad (4)$$

$$\eta_i = \text{proton or neutron}. \quad (5)$$

Here, the center  $\mathbf{X}_i$  of Gaussian is a complex number and treated as an independent free parameter for each nucleon. The width parameter  $\nu$  takes a common value for all nucleons, and is chosen to be an optimum value for each nucleus. The orientation of the intrinsic spin is expressed by a variational complex parameter  $\xi_i$ , and the isospin function is fixed to be up(proton) or down(neutron). Thus, an AMD wave function is specified by a set of variation parameters,  $\mathbf{Z} \equiv \{\mathbf{X}_1, \mathbf{X}_2, \dots, \mathbf{X}_A, \xi_1, \xi_2, \dots, \xi_A\}$ , which are optimized by the energy variation. As the variational wave function, we adopt the parity projected AMD wave function,

$$|\Phi_{\text{AMD}}^{\pm}\rangle = \frac{1 \pm P_x}{2} |\Phi_{\text{AMD}}\rangle. \quad (6)$$

Thus the parity projection is performed before the variation. This is essentially important to describe the parity asymmetric intrinsic structure such as the asymmetric cluster structure as discussed in Refs. [20,33].

## B. Hamiltonian and constraint

The Hamiltonian consists of the kinetic energy, nuclear and Coulomb forces. In the present work, we use the effective nuclear force consisting of two-body and three-body forces. Then the Hamiltonian is written as,

$$\hat{H} = \sum_i \hat{t}_i + \sum_{i < j} \hat{v}_{ij}^{(2)} + \sum_{i < j < k} \hat{v}_{ijk}^{(3)} - \hat{T}_{\text{cm}}, \quad (7)$$

where  $\hat{t}_i$  is a kinetic operator,  $\hat{v}^{(2)}$  and  $\hat{v}^{(3)}$  are two-body and three-body forces, respectively.  $\hat{T}_{\text{cm}}$  is the kinetic term for the center-of-mass motion. In the AMD wave function, the energy of center-of-mass motion is subtracted exactly.

We apply a constraint AMD method, where we find the minimum energy solution in the AMD model space under certain constraints. Since the particle-hole structure of the low-lying state is one of the main interests in the present work, we adopt the constraint of a total number of harmonic oscillator(H.O.) quanta,

$$\hat{N}_{\text{os}} \equiv \sum_i \left[ \frac{\mathbf{p}_i^2}{4\hbar^2\nu} + \nu \mathbf{r}_i^2 - \frac{3}{2} \right], \quad (8)$$

where the width parameter  $\nu$  is taken to be the same value as that of the single-particle wave packets in Eq.(3). This is the principal quantum number of the spherical harmonic oscillator with the oscillation number  $\omega = 2\hbar\nu/m$  ( $m$  is the nucleon mass). In order to obtain the minimum energy state with the constraint  $\langle \hat{N}_{\text{os}} \rangle = N_{\text{os}}$ , where  $N_{\text{os}}$  is a given number, we perform energy variation for the expectation value  $\mathcal{E}$  of the Hamiltonian,

$$\mathcal{E} \equiv \frac{\langle \Phi_{\text{AMD}}^{\pm} | \hat{H} | \Phi_{\text{AMD}}^{\pm} \rangle}{\langle \Phi_{\text{AMD}}^{\pm} | \Phi_{\text{AMD}}^{\pm} \rangle}, \quad (9)$$

with respect to the variational parameters  $\mathbf{Z}$  by the method of frictional cooling [20] under the constraint. We note the AMD wave function obtained with the energy variation for positive or negative parity state under the constraint  $\langle \hat{N}_{\text{os}} \rangle = N_{\text{os}}$  as  $\Phi_{\text{AMD}}(N_{\text{os}}^+)$  or  $\Phi_{\text{AMD}}(N_{\text{os}}^-)$ , respectively.

## C. superposition

In the obtained wave function  $\Phi_{\text{AMD}}(N_{\text{os}}^{(\pm)})$ , there exist local minimum solutions in the energy curve as a function of  $N_{\text{os}}$ . As shown later, those are usually the local minima also with respect to the deformation parameter  $\beta$  and considered to be approximate intrinsic wave functions for the corresponding deformed bands. In the calculation of level scheme and physical observables, we choose several intrinsic wave functions  $\Phi_{\text{AMD}}(k)$  and superpose the spin-parity projected wave functions,  $P_{MK}^J \Phi_{\text{AMD}}^{\pm}(k)$ , in order to satisfy the orthogonality among the calculated states and to obtain better wave functions. Here,  $k$  indicates  $N_{\text{os}}^{(\pm)}$  and stands for the label for the obtained intrinsic wave function ( $\Phi_{\text{AMD}}(k = N_{\text{os}}^{(\pm)})$ ). The wave function of the  $n$ th  $J^{\pm}$  state is written as,

$$\Psi_n^{J\pm} = \sum_{k,K} c_K^{J\pm}(k) P_{MK}^J \Phi_{\text{AMD}}^{\pm}(k), \quad (10)$$

where coefficients  $c_K^{J\pm}$  are determined by diagonalizing the Hamiltonian and norm matrices:

$$\langle P_{MK'}^J \Phi_{\text{AMD}}^{\pm}(k') | \hat{H} | P_{MK''}^J \Phi_{\text{AMD}}^{\pm}(k'') \rangle \quad \text{and} \quad (11)$$

$$\langle P_{MK'}^J \Phi_{\text{AMD}}^{\pm}(k') | P_{MK''}^J \Phi_{\text{AMD}}^{\pm}(k'') \rangle. \quad (12)$$

Physical quantity for an operator  $\hat{O}$  for the state is calculated as,

$$\langle \hat{O} \rangle = \langle \Psi_n^{J\pm} | \hat{O} | \Psi_n^{J\pm} \rangle. \quad (13)$$

If we use an enough number of base wave functions, this procedure of the superposition is equivalent to the generator coordinate method with respect to the generator coordinate  $N_{\text{os}}$ . However, the number of the basis in the superposition is 10 at most because of huge computational time in the numerical calculations of the total angular momentum projection in the present work. It means that  $\sum_k$  stands for the summation of discrete basis, and hence, the present calculations do not correspond to the complete GCM calculations.

### III. RESULTS

#### A. Effective nuclear force

We use an effective nuclear force which consists of central force, spin-orbit and Coulomb forces. As the central force, we use F3B force [30], which contains a finite-range three-body term. The parameter set (2) of the F3B force is adopted. As for the spin-orbit force, we use the same interaction as that adopted in Ref. [30], the two-range Gaussian spin-orbit term in G3RS force [34]. In the present calculations, the strength parameter of the spin-orbit force is chosen to be (i)  $u_{ls} \equiv u_1 = -u_2 = 2500$  MeV or (ii)  $u_{ls} = 1800$  MeV. Coulomb force is approximated by the sum of seven Gaussians.

In Fig. 1, we show the binding energies of  $Z = N$  nuclei from  ${}^4\text{He}$  to  ${}^{40}\text{Ca}$  obtained by using the present interaction parameters. The calculations are the simple AMD calculations without constraints. The binding energies calculated by variation after parity projection are shown in Fig. 1(a), and the energies with total-angular-momentum projection after the variation with parity projection are plotted in Fig. 1(b). We also show the results of Ref. [30] for the interaction(ii), where AMD calculations with constraint and superposition were performed. The energies for such deformed nuclei as  ${}^8\text{Be}$ ,  ${}^{12}\text{C}$ ,  ${}^{20}\text{Ne}$  and  ${}^{24}\text{Mg}$  are gained by the total-angular-momentum projection. As shown in Fig. 1(b), the binding energies of medium *sd* shell nuclei are overestimated by the interaction(i) due to the stronger spin-orbit force than that of the case(ii).

#### B. Shape coexistence

We apply the constraint AMD method to  ${}^{40}\text{Ca}$ . The width parameter  $\nu$  for the single-particle wave packets is chosen to be as  $\nu = 0.14 \text{ fm}^{-2}$  which optimizes the energy of the ground state. We impose the constraint of the total number of harmonic oscillator quanta as  $\langle \hat{N}_{\text{os}} \rangle = N_{\text{os}}$  on the parity projected AMD wave function, and obtain energy curves as a function of  $N_{\text{os}}$ . With a given constraint value  $N_{\text{os}}$ , we obtain a few states with different shapes as local minima. A prolate shape and an oblate shape are obtained by randomly choosing initial states in the variational procedure. In order to find possible cluster states, we also start the variation from initial states with various di-nuclear structure and decrease the  $N_{\text{os}}$ . Then we find that a  $\alpha + {}^{36}\text{Ar}$ -like clustering appears as a local minimum solution.

The energy curves as a function of the oscillator quanta( $N_{\text{os}}$ ) are shown in Figs.2 and 3. In principle, the minimum value of  $N_{\text{os}}$  for the positive-parity state is 60, which is given by the *sd*-shell-closed configuration, and it is 61 for negative-parity states. The results shown in the figure are calculated with the total-angular-momentum projected wave functions  $P_{MK}^J \Phi_{\text{AMD}}^{\pm}(N_{\text{os}}^{(\pm)})$ , where  $K = 0$  is chosen to obtain the lowest energy. The energies are also plotted as a function of quadrupole deformation  $\beta_2$ . Here the deformation parameter  $\beta_2$  is defined by using the sharp edge liquid drop relation between  $Q_2$  and  $\beta_2$  as follows;

$$\beta_2 = \sqrt{\frac{5}{16\pi}} \frac{4\pi Q_2}{3R^2 A} \quad (14)$$

$$Q_2 = 2\langle z^2 \rangle - \langle x^2 \rangle - \langle y^2 \rangle, \quad (15)$$

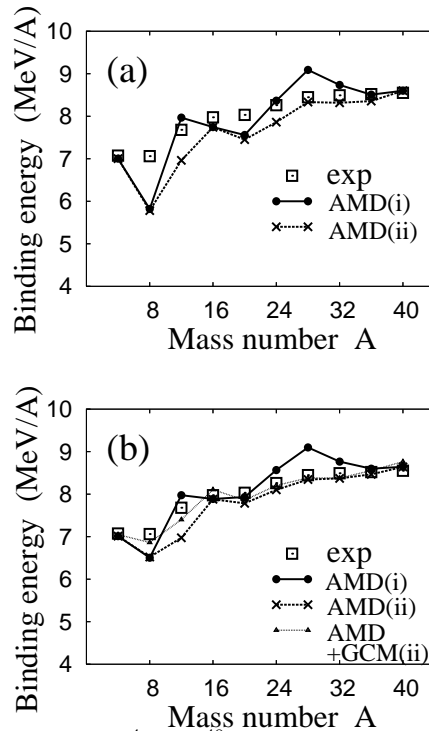


FIG. 1. The binding energies of  $Z = N$  nuclei from  ${}^4\text{He}$  to  ${}^{40}\text{Ca}$  obtained by the simple AMD calculations without constraints. The binding energies calculated by variation after parity projection but no total-angular-momentum projection are shown in the upper panel(a), and the energies obtained by total-angular-momentum projection after the variation with parity projection are plotted in the lower panel(b). Squares are the experimental binding energies. Filled circles and crosses indicate the results by using the interaction(i) and (ii), respectively. The results for the interaction(ii) in Ref. [30] of AMD calculations with constraint and superposition are shown by triangles with dotted line.

where the expectation values are calculated for the intrinsic states  $\Phi_{\text{AMD}}^{\pm}(N_{\text{os}}^{(\pm)})$ , and  $z$  is chosen to be an approximately symmetric axis. Here we use the fixed radius parameter,  $R$ , which is related to the nuclear mass  $A = 40$  according to the formula  $R = 1.2A^{1/3}$  fm.

We first mention the results of positive-parity states with the interaction(i) (Figs. 2(a) and (b)). We find three states with different shapes as the local minima on the energy surface. The lowest state in the  $J^\pi = 0^+$  curve is an almost spherical state at  $N_{\text{os}} = 62$ . There are two local minimum solutions in the energy curves, which almost degenerate to each other, at  $7 \sim 8$  MeV higher energy than the lowest solution. One is an oblate state at  $N_{\text{os}} \sim 65$  and the other is a large prolate deformation at  $N_{\text{os}} \sim 70$  with  $\beta_2 \sim 0.52$ . As shown later, the former contains a dominant  $4p\text{-}4h$  configuration, and the latter is dominated by a ‘ $8p\text{-}8h$ ’ configuration and corresponds to the superdeformed state. The appearance of the oblate state is consistent with the macroscopic-microscopic calculation [17] and also the 3d-HF calculations [16]. On the other hand, the calculated energy curve for the prolate states differs from the macroscopic-microscopic calculation by Leander and Larsson [17] where there is no local minimum for the  $8p\text{-}8h$  configuration but is a highly deformed  $12p\text{-}12h$  state. The  $\alpha + {}^{36}\text{Ar}$ -like cluster state appears in  $N_{\text{os}} \geq 69$  region, but it is much higher than the superdeformed state in the case of interaction(i). With a smaller  $N_{\text{os}}$  value of the constraint, the  $\alpha$ -cluster is absorbed into the  ${}^{36}\text{Ar}$  core and the  $\alpha + {}^{36}\text{Ar}$ -like state changes into the normal prolate state during the energy variation. In the  $2^+$  states, the energy curve for the prolate states is more gentle than the  $0^+$  curve at the small deformation region,  $0 < \beta_2 < 0.2$ .

Next we look into the results obtained with the interaction(ii) (Figs. 2(c) and (d)), which has the weaker spin-orbit force than the interaction(i). Although there exist the oblate state and the superdeformed state as local minima as same as in the results(i), the excitation energies of these states are much higher than those in the case of the interaction(i). The excitation energy of the superdeformed state is about 20 MeV, which largely overestimates the experimental energy, 5.21 MeV, of the bandhead of the superdeformed band. On the other hand, the energy of  $\alpha$ -cluster state does not so much change from (i) to (ii) because the effect of the spin-orbit force is smaller than other excited states. As a result,  $\alpha$ -cluster state almost degenerates with the superdeformed state and does not vanishes even in the smaller  $N_{\text{os}}$  region (as  $N_{\text{os}} \geq 66$ ) in the results(ii) than the case(i). Comparing Figs. 2(c) and (d), we find that the total number of H.O. quanta has a good correspondence with the quadrupole deformation  $\beta_2$  in the  $N_{\text{os}} \geq 64$  region for the prolate deformation. On the other hand, in the small  $N_{\text{os}}$  region, all the solutions for  $N_{\text{os}} \leq 63$  have almost spherical shapes with  $\beta_2 \sim 0$ . It means that different configurations with the same  $\beta_2$  value are obtained as optimum solutions for the given  $N_{\text{os}}$ .

We illustrate the density distribution of the intrinsic state  $\Phi_{\text{AMD}}(N_{\text{os}}^{(\pm)})$  in Fig.4 and Fig.5. A remarkable point is that parity asymmetric structure appears in the prolate states. Especially, one of striking features is the prominent cluster structure like  ${}^{12}\text{C} + {}^{28}\text{Si}$  in the large prolate deformation. Comparing the results of (i) and (ii), we remark that the intrinsic structure for a given  $N_{\text{os}}$  is almost the same as each other. It means that the structure of coexisting shapes is not sensitive to the choice of either interaction (i) or (ii) except for the  $\alpha$ -cluster state.

In contrast, the excitation energies strongly depend on the strength of the spin-orbit force as shown in the comparison between the results with a stronger spin-orbit force(i) and with a weaker one(ii). Particularly, the oblate state and the superdeformed state appear at the low excitation energies in the results with the interaction(i), but they exist at much higher excitation energies with the interaction(ii). Considering the  $4p\text{-}4h$  configuration in the oblate shape and the  ${}^{12}\text{C}\text{-}{}^{28}\text{Si}$  clustering in the superdeformed state, it is easily understood that the excitation energies of these states decrease with the stronger spin-orbit force(i) than with the weaker one(ii). Although the systematics of the binding energy in the  $sd$ -shell region seems to be reproduced better by the force(ii) than the force(i), however, the excitation energy of the superdeformed state is reasonably reproduced with the force(i) while they are largely overestimated by the force(ii). The force(i) also reproduces the excitation energy of the lowest negative-parity state ( $J^\pi = 3^-$ ) rather well than the force(ii) as shown later. Therefore, we examine mainly the results(i), because our interest is in excited states of  ${}^{40}\text{Ca}$ , especially in the properties of the superdeformed state. We should note again that the structure of the superdeformed state is stable in both cases (i) and (ii), and most of the intra-band properties of the superdeformed band does not so much depend on the choice of the interaction(i) or (ii) except for the relative energy to the ground state and other rotational bands.

Now we turn to negative-parity states. In Fig.3, we show the energies of  $J^\pi = 1^- (P_{MK}^{J=1} \Phi_{\text{AMD}}^-(N_{\text{os}}^{(-)}))$  and  $3^- (P_{MK}^{J=3} \Phi_{\text{AMD}}^-(N_{\text{os}}^{(-)}))$ , obtained with the interaction(i), as functions of (a)  $N_{\text{os}}$  and (b)  $\beta_2$ . It is found that the constraint on  $\langle \hat{N}_{\text{os}} \rangle$  acts as the constraint on deformation  $\beta_2$  in negative-parity states as well as in the positive-parity ones. In the small deformation region, the lowest state is the  $J^\pi = 3^-$  which corresponds to a  $1p\text{-}1h$  state. The difference between the minimum energy of the  $3^-$  state and that of the  $0^+$  state is 4.7 MeV, which well corresponds to the experimental excitation energy 3.74 MeV of the lowest  $3^-$  state. We here comment that the interaction (ii) gives a much larger energy difference as 6.9 MeV than the interaction (i) and fails to reproduce the experimental excitation energy of the  $3^-$  state. As  $N_{\text{os}}$  becomes large, the  $J^\pi = 1^-$  state becomes lower than the  $J^\pi = 3^-$  state and a  $K^\pi = 0^-$  rotational band with a prolate intrinsic state is built on this state. We illustrate the density distributions of

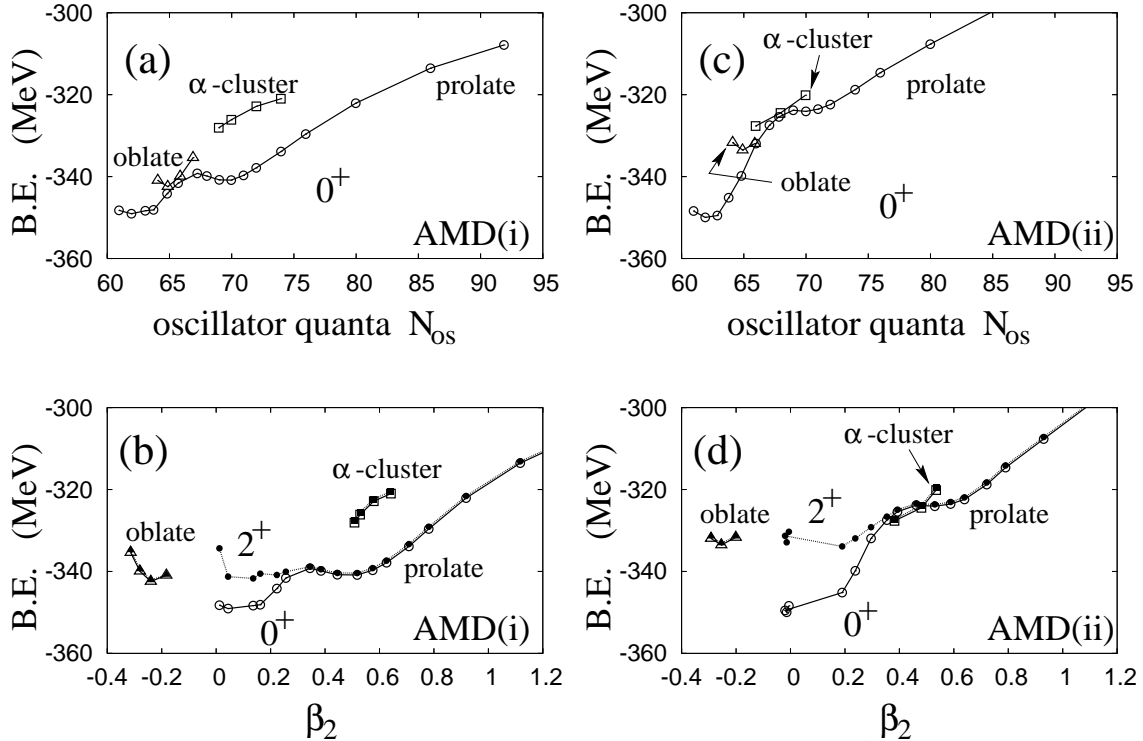


FIG. 2. The energy curves for the positive-parity states obtained by the constrained AMD calculations. The constraint of the total number of harmonic oscillator quanta,  $\langle \hat{N}_{\text{os}} \rangle = N_{\text{os}}$ , is imposed on the parity projected AMD wave function. The energies of the spin-parity projected states,  $P_{M0}^{J=0(2)} \Phi_{\text{AMD}}^{\pm}(N_{\text{os}}^{(\pm)})$ , are plotted (a)(c) as a function of  $N_{\text{os}}$  and (b)(d) as a function of deformation  $\beta_2$  of the states:  $\Phi_{\text{AMD}}^{\pm}(N_{\text{os}}^{(\pm)})$ . The left panels((a) and (b)) show the results with the interaction(i), and the right panels((c) and (d)) are for the results with the interaction(ii).

the intrinsic states for the negative parity states,  $\Phi_{\text{AMD}}(N_{\text{os}}^{(-)})$  in Fig.4(g)-(i). For each  $N_{\text{os}}$ , it is found that intrinsic structure of  $\Phi_{\text{AMD}}(N_{\text{os}}^{(-)})$  for the negative-parity state is quite similar to that of the prolate solution  $\Phi_{\text{AMD}}(N_{\text{os}}^{(+)})$  for the positive-parity state. In particular, the negative-parity state with  $N_{\text{os}} \geq 68$  has the parity-asymmetric shape because of the clustering which is regarded as the  $^{12}\text{C}+^{28}\text{Si}$ -like structure as well as the case of positive parity state. As a result, the largely deformed state forms the  $K^\pi = 0^-$  rotational band consisting of  $J^\pi = 1^-, 3^-, \dots$  due to the  $Y_{30}$  deformation, which may have a link to the positive-parity bands as a parity doublet.

### C. Energy levels

In the obtained wave function  $\Phi_{\text{AMD}}(N_{\text{os}}^{(\pm)})$ , there exist local minimum solutions in the energy curve as a function of  $N_{\text{os}}$ . They are also local minima with respect to the deformation  $\beta_2$  and considered to be approximate intrinsic wave functions for the corresponding deformed bands. In order to satisfy the orthogonality among the levels and to obtain better wave functions, we calculate the level scheme by superposing the spin-parity projected wave functions,  $P_{MK}^J \Phi_{\text{AMD}}^{\pm}(k)$ .

In the calculations with the case(i) interaction, we use  $N_{\text{os}}^{(\pm)} = 62^{(\pm)}, 65^{(\pm)}, 68^{(\pm)}, 70^{(\pm)}, 72^{(\pm)}, 76^{(\pm)}, 80^{(\pm)}, 86^{(\pm)}, 92^{(\pm)}$  with prolate shapes and  $N_{\text{os}}^{(\pm)} = 65_{\text{ob}}^{(\pm)}$  with the oblate shape as the basis for the positive-parity states. For the negative-parity states, we adopt  $N_{\text{os}}^{(\pm)} = 62^{(-)}, 63^{(-)}, 65^{(-)}, 66^{(-)}, 68^{(-)}, 69^{(-)}, 71^{(-)}, 65^{(+)}, 68^{(+)}, 65_{\text{ob}}^{(+)}$ . The obtained level scheme is shown in Fig.6. By analysing such properties as the dominant components and  $E2$  transition strengths of the obtained levels, we classify the levels into groups, which are labeled in Fig.6(b) and (c).

In the positive-parity levels, we find  $K^\pi = 0^+$  rotational bands corresponding to the shape coexistence:(B)the oblate band and (A3)the superdeformed band. The states in the groups (A1) and (A2) are built from the mixing of the spherical intrinsic state  $\Phi_{\text{AMD}}(N_{\text{os}} = 62^{(+)})$  and the normal prolate state  $\Phi_{\text{AMD}}(N_{\text{os}} = 65^{(+)})$ , while the side band (A2'(K=2)) of the normal deformation appears from the dominant  $P_{M2}^J \Phi_{\text{AMD}}^+(N_{\text{os}} = 65^{(+)})$  component due to the triaxial nature of the intrinsic state. In Fig.7, we plot the calculated excitation energies as a function of a spin

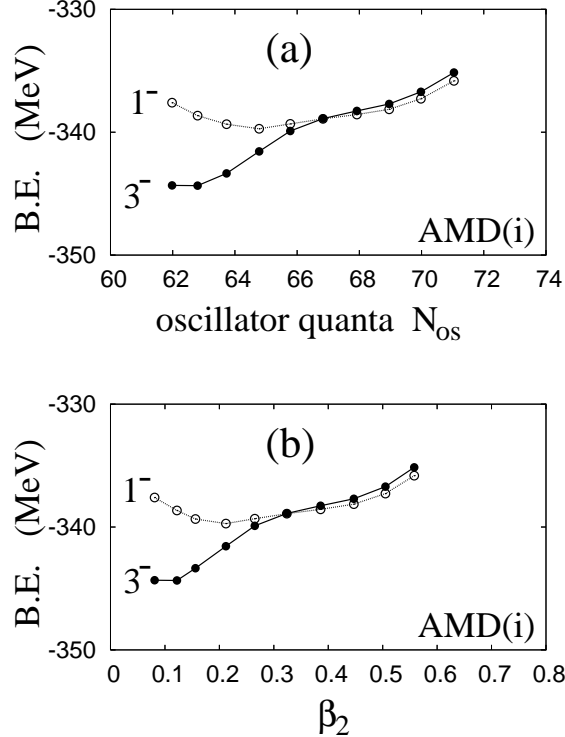


FIG. 3. The energy curves for the negative-parity states obtained by the constrained AMD calculations. The constraint of the total number of harmonic oscillator quanta,  $\langle \hat{N}_{\text{os}} \rangle = N_{\text{os}}$ , is imposed on the parity projected AMD wave function. The energies of the spin-parity projected states,  $P_{M0}^{J=1,3} \Phi_{\text{AMD}}^-(N_{\text{os}}^{(-)})$ , are plotted as a function of  $N_{\text{os}}$  in the upper panel(a) and as a function of the deformation  $\beta_2$  of  $\Phi_{\text{AMD}}^-(N_{\text{os}}^{(-)})$  in the lower panel(b). The results are obtained with the interaction(i).

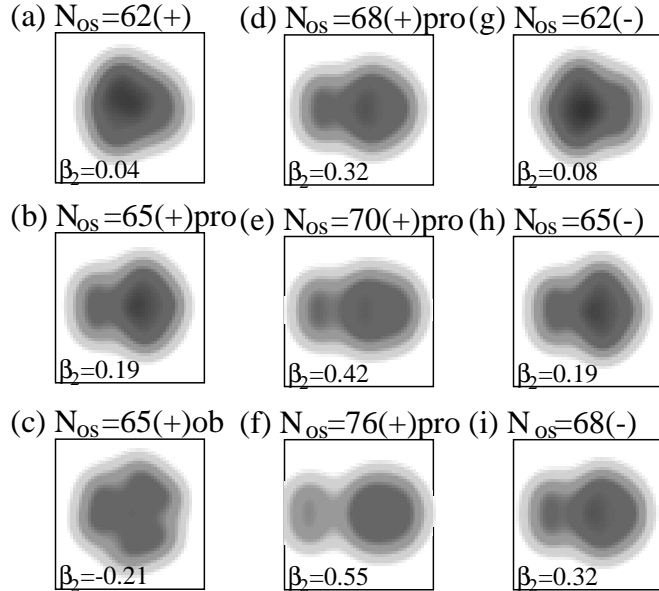


FIG. 4. Density distributions of the intrinsic states,  $\Phi_{\text{AMD}}(N_{\text{os}}^{(\pm)})$  for (a) the spherical state with  $N_{\text{os}}^{(\pm)} = 62^{(+)}$ , and the prolate solutions with  $N_{\text{os}}^{(\pm)} = (b) 65^{(+)}$ , (d)  $68^{(+)}$ , (e)  $70^{(+)}$ , (f)  $76^{(+)}$ , (g)  $62^{(-)}$ , (h)  $65^{(-)}$ , (i)  $68^{(-)}$ , and (c) the oblate solution with  $N_{\text{os}}^{(\pm)} = 65^{(+)}$ , which are obtained by using the interaction(i). The intrinsic system is projected onto the  $Y$ - $Z$  plane, and the density is integrated along the  $X$  axis, where  $X$ ,  $Y$  and  $Z$  axes are chosen as  $\langle X^2 \rangle \leq \langle Y^2 \rangle \leq \langle Z^2 \rangle$  and  $\langle XY \rangle = \langle YZ \rangle = \langle ZX \rangle = 0$ . The deformation parameters  $\beta_2$  are written at the bottom of the figures. The size of the frame is 10 fm  $\times$  10 fm.

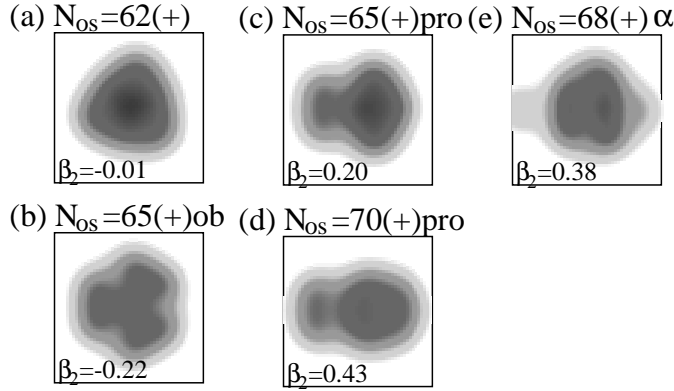


FIG. 5. Density distribution of the intrinsic states,  $\Phi_{\text{AMD}}(N_{\text{os}}^{(\pm)})$  for (a) the spherical state with  $N_{\text{os}}^{(\pm)} = 62^{(+)}$ , the prolate solutions with  $N_{\text{os}}^{(\pm)} = 65^{(+)}$  and (d)  $70^{(+)}$ , (b) the oblate solution with  $N_{\text{os}}^{(\pm)} = 65^{(+)}$ , and (e) the  $\alpha$ -cluster state with  $N_{\text{os}}^{(\pm)} = 68^{(+)}$ , which are obtained by using the interaction(ii). The intrinsic system is projected onto the  $Y$ - $Z$  plane, and the density is integrated along the  $X$  axis, where  $X$ ,  $Y$  and  $Z$  axes are chosen as  $\langle X^2 \rangle \leq \langle Y^2 \rangle \leq \langle Z^2 \rangle$  and  $\langle XY \rangle = \langle YZ \rangle = \langle ZX \rangle = 0$ . The deformation parameters  $\beta_2$  are written at the bottom of the figures. The size of the frame box is 10 fm  $\times$  10 fm.

$J(J+1)$ . We also show the experimental data of the bands labeled ‘‘band 2’’ and ‘‘band 1’’ in Ref. [12], which are assigned to be the normal-deformed band and the superdeformed band, respectively. Since the band (A2) contains the configuration mixing, the calculated level structure is not consistent with the rigid rotor levels and does not well agree to the experimental data of the normal-deformed band (labeled ‘‘band 2’’ in Ref. [12]). Moreover, it is higher than the superdeformed band in the present results(i), however, we tentatively assign this band as the normal-deformed band because of rather strong  $E2$  transitions in (A2) band. On the other hand, the calculated energy spectra of the superdeformed band behave as that of the rigid rotor and agrees to the experimental data for ‘‘band 1’’, though the excitation energy of the band-head state is slightly higher than the experimental data. The dominant components of the superdeformed band in the low-spin levels is  $P_{M0}^J \Phi_{\text{AMD}}^+(N_{\text{os}} = 70^{(+)})$ , which have a  $^{12}\text{C}+^{28}\text{Si}$ -like clustering. Another interesting character of the superdeformed band is its particle-hole property. As discussed later in detail,  $P_{M0}^J \Phi_{\text{AMD}}^+(N_{\text{os}} = 70^{(+)})$  has about 90% overlap with the band-head of the superdeformed band, and its intrinsic state  $\Phi_{\text{AMD}}(N_{\text{os}} = 70^{(+)})$  is regarded as a ‘‘8p-8h’’ state. This particle-hole feature of the superdeformed band is supported by the experimental fact that the  $0^+(5.21 \text{ MeV})$ ,  $2^+(5.63 \text{ MeV})$ , and  $4^+(6.54 \text{ MeV})$  in the superdeformed band are strongly populated in 8-nucleon-transfer reactions,  $^{32}\text{S}(^{12}\text{C},\alpha)^{40}\text{Ca}$  [11]. However, it is not consistent with the GCM calculations of Skyrme HF+BCS [18], where the superdeformed band can not be described by a certain  $np-nh$  configuration but contains a mixture of various configurations such as  $4p-4h$ ,  $6p-6h$ , and  $8p-8h$  states. In order to check the stability of the superdeformed band for the choice of the intrinsic wave functions to be superposed, we use another set of the basis as  $\{k\} = \{N_{\text{os}}^{(\pm)}\} = \{62^{(+)}, 64^{(+)}, 65^{(+)}, 66^{(+)}, 67^{(+)}, 68^{(+)}, 70^{(+)}, 72^{(+)}\}$  and find that the level scheme and the  $E2$  transition strengths in the superdeformed band are stable against the choice of the basis, and the properties of the states in bands (A1) and (A2) are qualitatively unchanged. In the present calculations, the number of the basis in the superposition is 10 at most and is much smaller than the GCM calculations in Ref. [18]. It also should be noted that, we did not obtain the basis with the quadrupole deformation  $0 < \beta_2 < 0.2$  as shown in Fig.2. For the detailed investigation of the band mixing, it is expected to be important to perform GCM calculations with a large number of the basis concerning the two-dimensional constraints on the  $N_{\text{os}}$  and  $\beta_2$ . The present results of the weak mixings between different  $np - nh$  configurations seem to be consistent with the experimental facts, however, we comment that the pairing correlations, which were taken into account in Ref. [18], are ignored in the present calculations though we think they are partially included through the spin-parity projections and superposition of the basis. Since the pairing correlations increase configuration mixings in general, it would be valuable to estimate the pairing effects on the stability of the superdeformed band.

In addition to the prolate bands, the oblate band appears at almost the same excitation energy as that of the superdeformed band. The moment of inertia is smaller than the superdeformed band. The oblate deformation is predicted also in the macroscopic-microscopic calculations [17] and in the mean-field calculations [18,16]. However, since an oblate band has not been experimentally assigned yet, the existence of an oblate shape in  $^{40}\text{Ca}$  is an open problem. We also find highly excited bands (A4) and (A5) which arise from the developed  $^{12}\text{C}+^{28}\text{Si}$  clustering. The details of these bands are discussed in the next section.

In the negative-parity states(Fig.6c), the lowest  $3^-$  and  $5^-$  states appear from almost the spherical states. The

theoretical excitation energies are in good agreement with the experimental data of the  $3_1^-$ (3.74 MeV) and the  $5_1^-$ (4.49 MeV). We find two  $K^\pi = 0^-$  rotational bands (C2) and (C3) which arise from the parity-asymmetric shape in the prolate states. Since the energies of the  $3^-$  and  $5^-$  states in these (C2) and (C3) bands are raised by the mixing with the lowest  $3^-$  and  $5^-$  states, the level structure is somehow out of that for the typical  $K^\pi = 0^-$  rotational band. The  $1_1^-$  state( $\Psi_{n=1}^{1-}$ ) in the band (C2) is dominated by  $P_{M0}^{J=1}\Phi_{\text{AMD}}^-(N_{\text{os}} = 65^{(-)})$  with the overlap  $|\langle\Psi_{n=1}^{1-}|P_{M0}^{J=1}\Phi_{\text{AMD}}^-(N_{\text{os}} = 65^{(-)})\rangle|^2 \sim 90\%$ , while the  $1_2^-$  state( $\Phi_{n=2}^{1-}$ ) in the band (C3) has the dominant  $P_{M0}^{J=1}\Phi_{\text{AMD}}^-(N_{\text{os}} = 69^{(-)})$  with 70% overlap. We should note that the  $1_1^-$  and  $1_2^-$  states have large overlap with also the  $1^-$  states projected from the intrinsic states for the positive-parity,  $\Phi_{\text{AMD}}(N_{\text{os}} = 65^{(+)})$  and  $\Phi_{\text{AMD}}(N_{\text{os}} = 68^{(+)})$ , respectively. It is reasonable because  $\Phi_{\text{AMD}}(N_{\text{os}}^{(-)})$  is almost the same state as the  $\Phi_{\text{AMD}}(N_{\text{os}}^{(+)})$  when the same constraint  $\langle\hat{N}_{\text{os}}\rangle = N_{\text{os}}$  is imposed. In order to find the possible parity doublet of the superdeformed band, we pay special attention to the  $\Phi_{\text{AMD}}(N_{\text{os}} = 68^{(+)})$  component in the largely deformed negative-parity band (C3) and in the superdeformed band (A3) with positive-parity. The overlap  $|\langle\Phi_{n=2}^{1-}|P_{M0}^{J=1}\Phi_{\text{AMD}}^-(N_{\text{os}} = 68^{(+)})\rangle|^2$  in the bandhead of the  $K^\pi = 0^-$  band(C3) is about 70%, while the bandhead  $0^+$  of the superdeformed band(A3) has 80% overlap with  $P_{M0}^{J=0}\Phi_{\text{AMD}}^+(N_{\text{os}} = 68^{(+)})$ . Then it leads to an interpretation that the largely deformed negative-parity band (C3) and the positive-parity superdeformed band (A3) are approximately the parity doublets  $K^\pi = 0^-$  and  $K^\pi = 0^+$  arising from the intrinsic state  $\Phi_{\text{AMD}}(N_{\text{os}} = 68^{(+)})$ , which has the parity asymmetric shape with the  $Y_{30}$  deformation due to the  $^{12}\text{C}+^{28}\text{Si}$ -like clustering as shown in Fig.4.

Next we discuss the energy levels calculated with the interaction(ii). We use  $N_{\text{os}}^{(\pm)} = 62^{(+)}, 65^{(+)}, 68^{(+)}, 70^{(+)}, 72^{(+)}$  with prolate deformations,  $N_{\text{os}}^{(\pm)} = 65_{\text{ob}}^{(+)}$  with the oblate shape, and  $N_{\text{os}}^{(\pm)} = 66_\alpha^{(+)}, 68_\alpha^{(+)}, 70_\alpha^{(+)}$  with  $\alpha$ -cluster-like structure as the basis in superposing  $P_{MK}^J\Phi_{\text{AMD}}^+(k)$ . The calculated excitation energies are shown in Fig.8. The rotational bands of oblate deformation, prolate one and superdeformation coexist as well as in the results(i). The excitation energies of these bands with the interaction(ii) are much higher than those of the results(i), and also are inconsistent with those of the experimentally known low-lying states. For example, the oblate band (B) starts from 17 MeV excitation energy, while the bandhead energy of the superdeformed band (A3) is 26 MeV. One of the characteristics of the results(ii) is that a  $\alpha$ -cluster-like band (D) appears at the relatively lower energy than the superdeformed band.

It has been known that the low-spin states in the normal-deformed band built on the  $0_2^+$ (3.35 MeV) state are strongly populated in  $\alpha$ -transfer reactions, and they have relatively larger  $\alpha$ -spectroscopic factors than other low-lying states [4–7]. Therefore, it is expected that the components of the  $\alpha$ -cluster state should be contained in the normal-deformed band. However, in the present calculations we failed to describe the  $\alpha$ -cluster components in the low-lying states, and even in the results(ii), the components of the  $\alpha$ -cluster state do not mix with the normal-deformed band (A2) except for the  $2^+$  state. It is because the energy difference between the bands (A2) and (D) are large in the present calculations. In order to solve this problem, it may be necessary to introduce a suitable nuclear interaction and extended model wave functions.

#### D. $E2$ transitions and moments

We calculate the  $E2$  transition strengths and the electric quadrupole moments for the excited states. We also extract quantities related to the intrinsic deformation from the physical observables such as  $B(E2)$  and electric quadrupole moments. By using the collective model approximation [35], we define the intrinsic quadrupole moment and the deformation by the  $E2$  transitions as,

$$Q_0^t = \sqrt{\frac{16\pi}{5e^2} \frac{B(E2, J_i \rightarrow J_f)}{\langle J_i K 20 | J_f K \rangle^2}}, \quad \beta^t = \sqrt{\frac{5}{16\pi} \frac{4\pi Q_0^t}{3R^2 Z}}, \quad (16)$$

where  $\langle J_i K 20 | J_f K \rangle$  is a Clebsch-Gordan coefficient.  $t$  stands for “transition”. We also extract the intrinsic quantities from the observable electric quadrupole moments  $Q$  as follows,

$$Q_0^s = \frac{1}{e} \frac{(J+1)(2J+3)}{3K^2 - J(J+1)} Q, \quad \beta^s = \sqrt{\frac{5}{16\pi} \frac{4\pi Q_0^s}{3R^2 Z}}. \quad (17)$$

Here  $s$  stands for “spectroscopic”.

In the table I, II and III, we show the calculated  $B(E2)$  and  $Q$  moments, and related quantities. The  $E2$  transitions are small among the states in the group (A1), which are dominated by spherical states and considered not to be a rotational band of a deformed state. On the other hand, the prolate band (A2) and the oblate one(B) have moderate transition strengths, while the  $E2$  transitions are remarkably strong in the superdeformed band (A3).

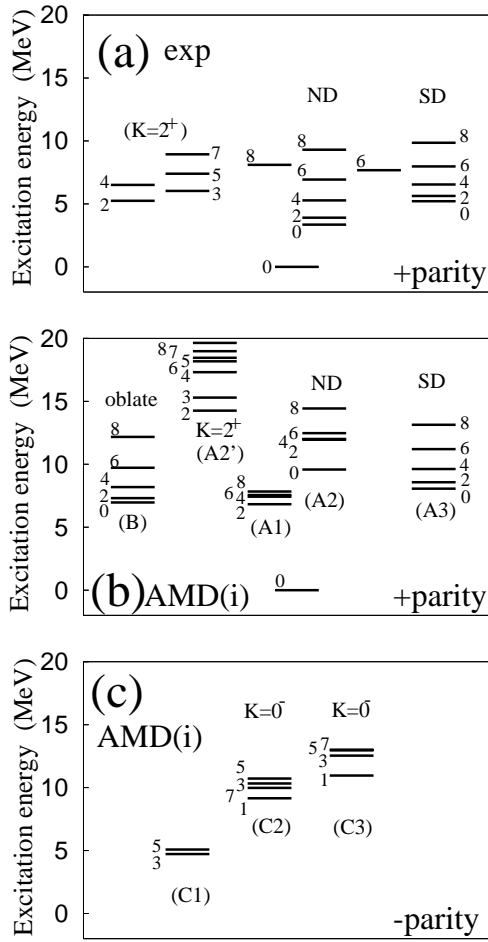


FIG. 6. Excitation energies of the levels up to  $J = 8$  in  $^{40}\text{Ca}$ . The experimental data of the levels observed in Ref. [12] are shown in (a). Figures (b) and (c) show the theoretical results for the positive-parity and negative-parity states, respectively, calculated by the superposition of the AMD wave functions. The interaction(i) is used. The excitation energies of the higher spin( $J > 8$ ) states will be shown in the next figures.

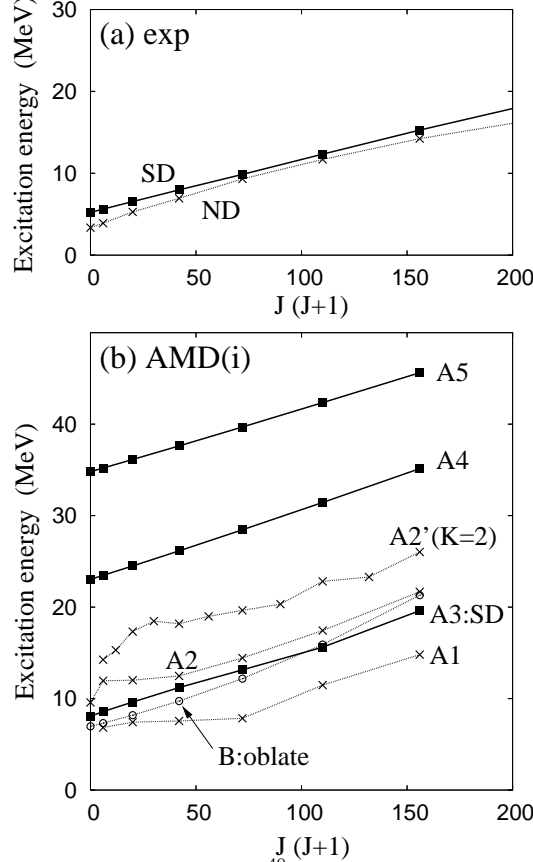


FIG. 7. Excitation energies of the positive-parity states in  $^{40}\text{Ca}$  as a function of a spin  $J(J+1)$ . Theoretical values shown in the lower panel (b) are those obtained with the interaction(i). The energies are calculated by the superposition of the AMD wave functions. The upper panel (a) shows the experimental data for the normal-deformed band and the superdeformed band, which are labeled “band 2” and “band 1” in Ref. [12], respectively.

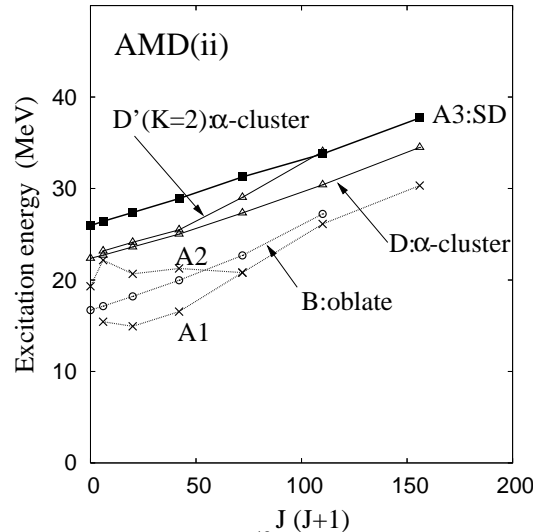


FIG. 8. Excitation energies of the positive-parity states in  $^{40}\text{Ca}$  obtained with the interaction(ii). The energies are calculated by the superposition of the AMD wave functions.

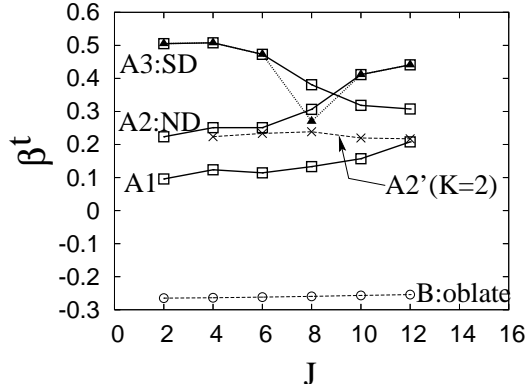


FIG. 9. The deformation parameters  $\beta^t$  extracted from the  $B(E2)$  values for the intra-band transitions. The labels of the bands correspond to those in Fig.6. The results are for the calculations with the interaction(i).

In the results with the interaction(i), the deformation parameter  $\beta^t$  extracted from the  $B(E2)$  is consistent with  $\beta^s$  evaluated with the  $Q$  moment except for negative-parity bands and high spin states in the prolate bands (A1), (A2), and (A3). In Fig.9, we show the behavior of the transition deformation  $\beta^t$  with the increase of the total-angular momentum  $J$ . In the oblate band (B), the intrinsic deformation  $\beta$  is almost constant with the increase of  $J$ , because the oblate states do not mix with the other shapes. On the other hand,  $\beta^t$  in the bands (A1), (A2) and (A3) changes as  $J$  increases. The deformation of the low-spin states in the superdeformed band (A3) decreases, while that of the normal-deformed band (A2) enlarges, and the  $\beta^t$ -lines for these two bands cross each other around  $J = 8$ . We remark that the state mixing occurs in the region  $J \geq 6$ , and the components contained in (A2) and (A3) change around  $J = 8$ . As a result, the transition from the  $8^+(A2)$  to  $6^+(A3)$  is significant strong(see Table I). Therefore, another assignment may be possible as  $8^+(A2)$ ,  $10^+(A2)$  and  $12^+(A2)$  belong to the superdeformed band. In fact,  $\beta^t$  extracted from the  $B(E2; J \rightarrow J-2)$  among the  $0^+(A3)$ ,  $2^+(A3)$ ,  $4^+(A3)$ ,  $6^+(A3)$ ,  $8^+(A2)$ ,  $10^+(A2)$  and  $12^+(A2)$  are so large as shown by filled triangles in Fig.9, that these states can be assigned to compose a rotational band with the strong  $E2$  transitions. In the experimental data by Ideguchi et al. [?], they observed the deviation from the constant moment of inertia in the superdeformed band and also the inter-band gamma transitions between normal deformation and superdeformation. These facts may give an indication of the possible band mixing or some structure change around  $J \sim 8$  in the superdeformation. Further fine measurements of  $E2$  transition strengths will be helpful to see the details of the band mixing and to establish the assignment for the high spin states of the superdeformed band.

In the results with the interaction(ii) (table III), we also find strong  $E2$  transitions in the superdeformed band (A3). The transitions of the prolate band (A2) are weaker in the results(ii) than in the case(i). As mentioned before, the  $K^\pi = 0^+(D)$  and  $K^\pi = 2^+(D')$  bands with the  $\alpha$ -cluster structure appear below the superdeformed band in the results(ii). These bands have strong intra-band  $E2$  transitions, which give the larger transition deformations  $\beta^t \approx 0.4$  than the prolate band (A2).

Let us make a comparison of intra-band transitions between the present results and the experimental data, and also compare them with other theoretical calculations. The theoretical and experimental values of  $Q_0^t$  for the normal-deformed band and the superdeformed band are listed in table IV. The present results for the superdeformed band are in reasonable agreements with the experimental data. They are also consistent with the results by GCM+HFBCS calculations. In the shell model calculations by Poves *et al.*, large  $Q_0^t$  values were obtained with the truncated calculations within  $8p-8h$  configurations by using effective charges  $q_\pi = 1.5$  and  $q_\nu = 0.5$  for protons and neutrons, however, the  $Q_0^t$  get eroded when other particle-hole configurations are mixed in the calculations. The  $Q_0^t$  moments of the band (A2) are  $Q_0^t = 57 - 112 \text{ fm}^2$  and comparable to the experimental values  $Q_0^t = 74 \pm 14 \text{ fm}^2$  for the normal deformation(band 2) in Ref. [12], but are smaller than the experimental data  $Q_0^t = 1.1 \pm 0.1 \times 10^2$  and  $1.3 \pm 0.2 \times 10^2 \text{ fm}^2$  in Ref. [36]. Our results are consistent with the GCM+HFBCS calculations except for the  $4^+$  state, which has a small  $Q_0^t$  in the GCM+HFBCS result. As shown in table III, we obtain the  $\alpha$ -cluster band (D) with strong  $E2$  transitions in case of the interaction(ii). The transition moment of the band (D) is  $Q_0^t \approx 100 \text{ fm}^2$  and well agrees to the experimental data in Ref. [36]. Therefore, there might be an alternative assignment that the band (D) corresponds to the normal-deformed band built on the  $0_2^+(3.35 \text{ MeV})$ , though the excitation energy of the band (D) is much higher than the experimental data in the present calculations.

The  $K = 2$  band were experimentally established based on the measurement of  $B(E2)$  [1,37]. The observed intra-band transitions are  $B(E2; 3^+ \rightarrow 2^+) = 730 \pm 300 (e^2 \text{ fm}^4)$  and  $B(E2; 4^+ \rightarrow 2^+) = 200 + 150 - 75 (e^2 \text{ fm}^4)$  [1]. The properties of this band were studied by Sakuda and Ohkubo with  $\alpha + {}^{36}\text{Ar}(2^+)$ -cluster model [9,10], which well

replicates these intra-band transitions. In the present calculations, we find the  $K^\pi = 2^+$  band (A2') with the prolate deformation in the results(i), and the  $K^\pi = 2^+$  band (D') with the  $\alpha$ -cluster structure in the case of (ii). In the band (A2'), the calculated  $E2$  transition strengths are  $B(E2; 3^+ \rightarrow 2^+ = 95 \text{ (e}^2 \text{ fm}^4)$  and  $B(E2; 4^+ \rightarrow 2^+ = 38 \text{ (e}^2 \text{ fm}^4)$ , which are smaller than experimental  $B(E2)$  values. On the other hands, the  $E2$  transition strengths in the band (D') are large enough as  $B(E2; 3^+ \rightarrow 2^+) = 390 \text{ (e}^2 \text{ fm}^4)$  and  $B(E2; 4^+ \rightarrow 2^+) = 129 \text{ (e}^2 \text{ fm}^4)$ , which well correspond to the data within the experimental error bars. It means that the deformation of the  $K = 2$  band can be described by the  $\alpha$ -cluster band (D'), which is obtained with the interaction (ii).

Next we discuss the moments of the negative-parity states. For the negative-parity states in the group (C1), the magnetic dipole moments of the  $3^-$  and  $5^-$  states are  $\mu(3^-) = 1.66 \mu_N$  and  $\mu(5^-) = 2.76 \mu_N$ , which well agree to the experimental values for the lowest  $3_1^-$  (3.74 MeV) and the lowest  $5_1^-$  (4.49 MeV);  $\mu(3_1^-) = 1.65 \mu_N$  and  $\mu(5^-) = 2.6 \mu_N$ . In the prolate bands (C2) and (C3), the  $E2$  transitions are fragmented among the bands because the  $3^-$  and  $5^-$  states of these bands contain configuration mixing due to the existence of the lowest  $3^-$  and  $5^-$  states in the group (C1) (see table II). Then, we estimate the intrinsic deformation by looking into  $\beta^s$  extracted from the  $Q$  moments instead of  $\beta^t$ . According to the calculated  $\beta^s$  of the band-head state( $1^-$ ), the deformation of the band (C3) is evaluated as  $\beta^s = 0.39$ . This is smaller than that of the superdeformed band (A3), which we roughly assign to the parity doublet of (C3).

## IV. DISCUSSION

### A. Molecular bands

Appearance of molecular resonances is one of the important cluster aspects in *sd*-shell nuclei. In the large prolate deformations of  $^{40}\text{Ca}$ , we find the trend of developed  $^{12}\text{C}+^{28}\text{Si}$  clustering which leads to the superdeformed band as mentioned in the previous section. Therefore, it is natural to expect possible existence of  $^{12}\text{C}+^{28}\text{Si}$  molecular bands and their link with the superdeformed band in  $^{40}\text{Ca}$ .

It has been known that molecular resonances appear in such systems as  $^{12}\text{C}+^{12}\text{C}$ ,  $^{12}\text{C}+^{16}\text{O}$  or  $^{16}\text{O}+^{16}\text{O}$  [38,39]. In the microscopic calculations, there have been theoretical efforts to connect the molecular resonances with the low-lying deformed bands [22,40–42]. We should stress that the recent AMD studies [22,42] are the first theoretical works which can microscopically describe both the coexisting deformed states in low-energy region and the molecular resonances in the high-energy region without relying on assumptions of constituent clusters. In Ref. [22], the relation between the theoretically predicted superdeformed band in  $^{32}\text{S}$  and the  $^{16}\text{O}+^{16}\text{O}$  molecular bands has been studied. It has been suggested that the superdeformed band with a considerable amount of the  $^{16}\text{O}+^{16}\text{O}$  component is regarded as the lowest nodal band in a series of  $^{16}\text{O}+^{16}\text{O}$  molecular bands, while the excited  $^{16}\text{O}+^{16}\text{O}$  bands arise due to the inter-cluster excitation and correspond to the observed molecular resonances.

In the present results of the case(i), we find the excited rotational bands (A4) and (A5) as shown in Fig.7. The former and the latter exist at about 15 MeV and 25 MeV higher excitation energies than that of the superdeformed band, respectively. These bands appear due to the superposition of the large prolate deformations with the  $^{12}\text{C}+^{28}\text{Si}$  cluster structure. In Fig.10, we show the overlap of the states( $\Psi_n^{J+}$ ) in the prolate bands (A1), (A2), (A3), (A4) and (A5) with a single AMD state:  $|\langle \Psi_n^{J+} | P_{M0}^J \Phi_{\text{AMD}}^\pm(N_{\text{os}}^{(+)}) \rangle|^2$ . The low-spin( $J \leq 4$ ) states in the superdeformed band is dominated by  $P_{M0}^J \Phi_{\text{AMD}}^\pm(N_{\text{os}} = 70^{(+)})$  with about 90% overlap. We should stress again that the  $^{12}\text{C}+^{28}\text{Si}$ -like clustering actually appears in the  $\Phi_{\text{AMD}}(N_{\text{os}} = 70^{(+)})$  (see Fig.4). On the other hand, the states in the excited band (A4) contain the AMD states with larger  $N_{\text{os}}$ , and the components in the band (A5) shift toward the further large  $N_{\text{os}}$  region. Since the di-nuclear clustering develops further and two clusters go away from each other with the increase of  $N_{\text{os}}$ , these excited bands (A4) and (A5) should be described by the excitation of inter-cluster motion. In fact, we calculate the oscillator quanta of the subsystem consisting of the nucleons within each cluster( $^{12}\text{C}$  or  $^{28}\text{Si}$ ), and find that each of the cluster is almost written by  $0\hbar\omega$  configurations. In other words, the increase of  $N_{\text{os}}$  corresponds to just enlarging the inter-cluster distance, and hence, the rotational bands (A4) and (A5) arise due to the excitation of relative motion between  $^{12}\text{C}$  and  $^{28}\text{Si}$  clusters. Moreover, it is suggested that the bands (A4) and (A5) may have tails in the inter-cluster motion because the components of these bands are spread into the broader  $N_{\text{os}}$  ranges than that of the superdeformed band. These results suggest an interpretation that the superdeformed band (A3) and the higher bands (A4) and (A5) are regarded as a series of  $^{12}\text{C}+^{28}\text{Si}$  molecular bands. Namely, the bands (A4) and (A5) appear as the higher nodal states built above the the superdeformed band. These results have a good analogy to the feature of the superdeformed band and the  $^{16}\text{O}+^{16}\text{O}$  bands in  $^{32}\text{S}$  discussed in Ref. [22].

In the experimental side, the  $^{12}\text{C}+^{28}\text{Si}$  resonances have been observed in the elastic scattering data in the backward-angle region [24,38]. The resonances at the energy  $E_{\text{cm}} = 26.0$  and  $30.2$  MeV, which correspond to the excited states of  $^{40}\text{Ca}$  at  $E = 39$  and  $44$  MeV, are assigned to be  $J = 18$  states from the angular distributions. There

TABLE I. Electric quadrupole moments  $Q$  ( $e \text{ fm}^2$ ) and  $B(E2)$  ( $e^2 \text{ fm}^4$ ) for the positive-parity states calculated with the interaction(i). The extracted intrinsic quadrupole moments ( $\text{fm}^2$ ) and deformation parameters are also listed. The definitions of  $Q_0^{t,s}$  and  $\beta^{t,s}$  are explained in the text. The labels of the bands correspond those in Fig.6.

$J^\pi$	band	$Q$	$Q_0^s$	$\beta^s$	transition to final	band	$B(E2)$	$Q_0^t$	$\beta^t$
positive-parity bands									
$2^+$	(A1)	-10	34	0.13	$0^+$	(A2)	12	24	0.10
$4^+$	(A1)	-10	28	0.11	$2^+$	(A1)	28	31	0.12
$6^+$	(A1)	-13	33	0.13	$4^+$	(A1)	27	29	0.11
$8^+$	(A1)	-15	36	0.14	$6^+$	(A1)	38	34	0.13
$10^+$	(A1)	-22	50	0.19	$8^+$	(A1)	54	40	0.16
$12^+$	(A1)	-30	68	0.27	$10^+$	(A1)	96	53	0.21
prolate									
$2^+$	(A2)	-17	61	0.24	$0^+$	(A2)	64	57	0.22
$4^+$	(A2)	-24	65	0.26	$2^+$	(A2)	116	64	0.25
$6^+$	(A2)	-29	72	0.28	$4^+$	(A2)	128	64	0.25
$8^+$	(A2)	-43	102	0.40	$6^+$	(A2)	200	78	0.31
$8^+$	(A2)				$6^+$	(A3)	161	70	0.27
$10^+$	(A2)	-50	116	0.45	$8^+$	(A2)	370	105	0.41
$12^+$	(A2)	-56	126	0.49	$10^+$	(A2)	433	112	0.44
superdeformation									
$2^+$	(A3)	-37	131	0.51	$0^+$	(A3)	330	129	0.51
$4^+$	(A3)	-47	129	0.51	$2^+$	(A3)	476	129	0.51
$6^+$	(A3)	-47	118	0.46	$4^+$	(A3)	455	121	0.47
$8^+$	(A3)	-40	95	0.37	$6^+$	(A3)	309	97	0.38
$10^+$	(A3)	-36	83	0.33	$8^+$	(A3)	222	81	0.32
$12^+$	(A3)	-43	97	0.38	$10^+$	(A3)	210	78	0.31
oblate									
$2^+$	(B)	19	-67	-0.26	$0^+$	(B)	91	-68	-0.26
$4^+$	(B)	24	-66	-0.26	$2^+$	(B)	128	-67	-0.26
$6^+$	(B)	25	-63	-0.25	$4^+$	(B)	139	-67	-0.26
$8^+$	(B)	25	-60	-0.24	$6^+$	(B)	143	-66	-0.26
$10^+$	(B)	25	-57	-0.22	$8^+$	(B)	144	-65	-0.26
$12^+$	(B)	23	-52	-0.21	$10^+$	(B)	144	-65	-0.25
$K = 2$ band									
$2^+$	(A2';K=2)	13	47	0.18					
$3^+$	(A2';K=2)				$2^+$	(A2';K=2)	95	52	0.20
$4^+$	(A2';K=2)	-9	61	0.24	$2^+$	(A2';K=2)	38	57	0.22
$5^+$	(A2';K=2)	-12	53	0.21	$3^+$	(A2';K=2)	25	36	0.14
$6^+$	(A2';K=2)	-18	62	0.24	$4^+$	(A2';K=2)	83	60	0.23
$7^+$	(A2';K=2)	-20	63	0.25	$5^+$	(A2';K=2)	58	47	0.18
$8^+$	(A2';K=2)	-22	63	0.25	$6^+$	(A2';K=2)	104	61	0.24
$9^+$	(A2';K=2)	-24	64	0.25	$7^+$	(A2';K=2)	113	62	0.24
$10^+$	(A2';K=2)	-22	57	0.22	$8^+$	(A2';K=2)	96	56	0.22
$11^+$	(A2';K=2)	-25	63	0.25	$9^+$	(A2';K=2)	114	60	0.24
$12^+$	(A2';K=2)	-28	67	0.26	$10^+$	(A2';K=2)	99	55	0.22

TABLE II. Electric quadrupole moments  $Q$  ( $e \text{ fm}^2$ ) and  $B(E2)$  ( $e^2 \text{ fm}^4$ ) for the negative-parity states calculated with the interaction(i). The extracted intrinsic quadrupole moments ( $\text{fm}^2$ ) and deformation parameters are also listed. The definitions of  $Q_0^{t,s}$  and  $\beta^{t,s}$  are explained in the text. The labels for the bands are the same as those in Fig.6.

$J^\pi$	band	$Q$	$Q_0^s$	$\beta^s$	transition to final	band	$B(E2)$	$Q_0^t$	$\beta^t$
negative-parity bands									
$3^-$	(C1)	-9	27	0.11					
$5^-$	(C1)	-10	25	0.10	$3^-$	(C1)	25	29	0.11
prolate									
$1^-$	(C2)	-12	59	0.23					
$3^-$	(C2)	-29	88	0.35	$1^-$	(C2)	89	59	0.23
$3^-$	(C2)				$1^-$	(C3)	133	72	0.28
$5^-$	(C2)	-31	81	0.32	$3^-$	(C2)	209	83	0.33
$7^-$	(C2)	-22	53	0.21	$5^-$	(C2)	76	49	0.19
$7^-$	(C2)				$5^-$	(C1)	26	28	0.11
large prolate									
$1^-$	(C3)	-20	100	0.39					
$3^-$	(C3)	-28	85	0.34	$1^-$	(C3)	150	76	0.30
$5^-$	(C3)	-34	88	0.35	$3^-$	(C3)	216	85	0.33
$7^-$	(C3)	-40	98	0.38	$5^-$	(C3)	178	74	0.29
$7^-$	(C3)				$5^-$	(C2)	150	68	0.27

are other experimental implications of  $^{12}\text{C}+^{28}\text{Si}$  molecular states in the low-energy fusion cross section [23], where distinct structures have been found in the energy region  $E_{\text{cm}}=20-30$  MeV above the  $^{12}\text{C}+^{28}\text{Si}$  threshold. These are the candidates of the molecular resonances which might correspond to the  $^{12}\text{C}+^{28}\text{Si}$  molecular bands (A4) and (A5) obtained in the present results. In order to make further investigations of the molecular bands and give more quantitative discussions, it should be important to superpose a large number of the AMD states. It also may be effective to take into account the excitation inside the clusters as coupled channel calculations for the description of the detailed band structure.

## B. single-particle orbits

In an AMD wave function, the single-particle wave packets,  $\varphi_i$ , in Eq.(3) are not orthogonal to each other. In order to study the mean-field character, it is useful to transform them to the HF-like single-particle orbits  $\{\varphi_a^{\text{HF}}\}$ , which are orthonormal to each other and form the total wave function equivalent to the original AMD wave function. We extracted the single-particle orbits  $\{\varphi_a^{\text{HF}}\}$  from  $\Phi_{\text{AMD}}(N_{\text{os}}^{(\pm)})$ , as explained in Refs [32,43], and analyze them.

As mentioned before, the low-spin states of the superdeformed band is dominated by the AMD state,  $P_{M_0}^J \Phi_{\text{AMD}}^+(N_{\text{os}} = 70^{(+)})$ . We find that the intrinsic state,  $\Phi_{\text{AMD}}(N_{\text{os}} = 70^{(+)})$ , contains eight  $fp$ -like single-particle levels, which are the highest 4 levels among proton orbits and the highest 4 levels among the neutron orbits. Each of these levels has dominant parity-odd component as the ratio  $P(-) \sim 95\%$ . The density distributions of these levels are shown in Fig.11(a) and (b). Hereafter, we use the label  $a=(1,\dots,20)$  of  $\{\varphi_a^{\text{HF}}\}$  for the  $a$ th highest single-particle levels in the proton orbits. It is found that the properties of the eight valence levels in  $\Phi_{\text{AMD}}(N_{\text{os}} = 70^{(+)})$  are associated with the longitudinal  $fp$  orbits which have  $Y_{3,\pm 1}$  and  $Y_{3,0}$  angular dependent terms. Therefore, we regard the superdeformed state as a “8p-8h” state, though it is not equivalent to pure particle-hole states in the mean-field picture. The origin of the parity asymmetric shape with  $^{12}\text{C}+^{28}\text{Si}$  cluster in  $\Phi_{\text{AMD}}(N_{\text{os}} = 70^{(+)})$  will be discussed later.

The prolate band (A2) contains the significant component of the AMD state projected from the intrinsic state,  $\Phi_{\text{AMD}}(N_{\text{os}} = 65^{(+)})$ . The valence orbits in this state are the eight levels which contain 50% parity-odd components and 50% parity-even ones as shown in figures 11(d) and (e). It means that the parity projected state  $\Phi_{\text{AMD}}^+(N_{\text{os}} = 65^{(+)})$  can be approximately described by the mixing of  $2p-2h$ ,  $4p-4h$  and  $6p-6h$  configurations. We comment that  $\Phi_{\text{AMD}}(N_{\text{os}} = 65^{(+)})$  is not a local minimum in the energy curve as a function of  $N_{\text{os}}$  nor  $\beta$ .

The oblate solution  $\Phi_{\text{AMD}}(N_{\text{os}} = 65_{\text{ob}}^{(+)})$  does not mix with the prolate states, and independently forms the oblate band (B). This state can be convincingly described by a  $4p-4h$  state because 4 valence nucleons occupy almost parity-

TABLE III. Electric quadrupole moments  $Q$  ( $e \text{ fm}^2$ ) and  $B(E2)$  ( $e^2 \text{ fm}^4$ ) calculated with the interaction(ii). The extracted intrinsic quadrupole moments ( $\text{fm}^2$ ) and deformation parameters are also listed. The definitions of  $Q_0^{t,s}$  and  $\beta^{t,s}$  are explained in the text. The labels for the bands correspond to those in Fig.8.

$J^\pi$	band	$Q$	$Q_0^s$	$\beta^s$	transition to		$B(E2)$	$Q_0^t$	$\beta^t$
					final	band			
$2^+$	(A1)	-8	29	0.11	$0^+$	(A2)	27	37	0.14
$4^+$	(A1)	-2	7	0.03	$2^+$	(A1)	9	18	0.07
$6^+$	(A1)	-7	18	0.07	$4^+$	(A1)	2	8	0.03
prolate									
$2^+$	(A2)	-14	48	0.19	$0^+$	(A2)	48	49	0.19
$4^+$	(A2)	-21	57	0.22	$2^+$	(A2)	60	46	0.18
$6^+$	(A2)	-21	53	0.21	$4^+$	(A2)	89	53	0.21
$8^+$	(A2)	-23	54	0.21	$6^+$	(A2)	88	52	0.20
$10^+$	(A2)	-29	67	0.26	$8^+$	(A2)	121	60	0.23
$12^+$	(A2)	-32	72	0.28	$10^+$	(A2)	161	69	0.27
superdeformation									
$2^+$	(A3)	-40	138	0.54	$0^+$	(A3)	382	139	0.54
$4^+$	(A3)	-49	135	0.53	$2^+$	(A3)	524	136	0.53
$6^+$	(A3)	-52	129	0.51	$4^+$	(A3)	528	130	0.51
$8^+$	(A3)	-49	116	0.45	$6^+$	(A3)	476	120	0.47
$10^+$	(A3)	-49	113	0.44	$8^+$	(A3)	363	104	0.41
$12^+$	(A3)	-54	120	0.47	$10^+$	(A3)	383	106	0.41
oblate									
$2^+$	(B)	20	-71	-0.28	$0^+$	(B)	102	-72	-0.28
$4^+$	(B)	25	-68	-0.27	$2^+$	(B)	145	-71	-0.28
$6^+$	(B)	26	-66	-0.26	$4^+$	(B)	157	-71	-0.28
$8^+$	(B)	26	-62	-0.24	$6^+$	(B)	161	-70	-0.27
$10^+$	(B)	23	-52	-0.21	$8^+$	(B)	155	-68	-0.27
$\alpha$ -cluster									
$2^+$	(D)	-29	101	0.40	$0^+$	(D)	195	99	0.39
$4^+$	(D)	-34	92	0.36	$2^+$	(D)	289	101	0.40
$6^+$	(D)	-41	103	0.41	$4^+$	(D)	309	99	0.39
$8^+$	(D)	-27	63	0.25	$6^+$	(D)	271	91	0.36
$10^+$	(D)	-26	61	0.24	$8^+$	(D)	420	112	0.44
$12^+$	(D)	-28	64	0.25	$10^+$	(D)	440	113	0.44
$K = 2:\alpha$ -cluster									
$2^+$	(D';K=2)	31	110	0.43	$0^+$	(D';K=2)			
$3^+$	(D';K=2)				$2^+$	(D';K=2)	390	105	0.41
$4^+$	(D';K=2)	-20	139	0.55	$2^+$	(D';K=2)	129	104	0.41
$5^+$	(D';K=2)	-24	106	0.41	$3^+$	(D';K=2)	216	107	0.42
$6^+$	(D';K=2)	-30	104	0.41	$4^+$	(D';K=2)	202	93	0.37
$7^+$	(D';K=2)	-33	101	0.40	$5^+$	(D';K=2)	237	95	0.37
$8^+$	(D';K=2)	-50	143	0.56	$6^+$	(D';K=2)	152	73	0.29
$9^+$	(D';K=2)	-35	94	0.37	$7^+$	(D';K=2)	267	95	0.37
$10^+$	(D';K=2)	-59	152	0.59	$8^+$	(D';K=2)	250	90	0.35

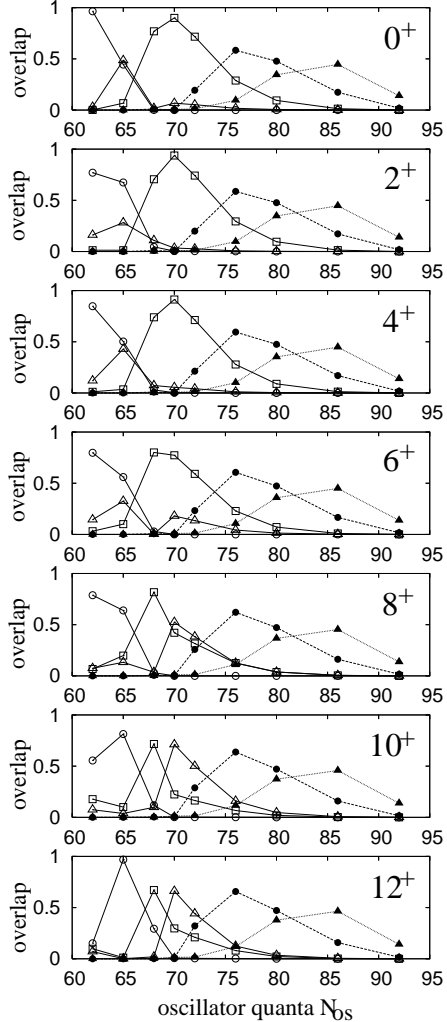


FIG. 10. The overlap between the calculated excited states  $\Psi_n^{J+}$  and the prolate AMD states  $P_{M0}^J \Phi_{\text{AMD}}^+(N_{\text{os}}^{(+)})$ . The values  $|\langle \Phi_n^{J+} | P_{M0}^J \Phi_{\text{AMD}}^+(N_{\text{os}}^{(+)}) \rangle|^2$  for the states in the bands (A1), (A2), (A3), (A4) or (A5) are shown by open circles, open triangles, open squares, filled circles or filled triangles, respectively.

TABLE IV. Intrinsic quadrupole moments ( $\text{fm}^2$ ) of the normal-deformed band and the superdeformed band extracted from  $B(E2)$  with the definition in Eq.(16). The present AMD results for the normal-deformed band and the superdeformed band are those for the bands (A2) and (A3) with the interaction(i), respectively. The values in parenthesis are those for the assignment of the  $8^+, 10^+, 12^+$  states in the band (A2) to the superdeformed states. The shell model calculations by Poves *et al.* [19], and the GCM+HFBCS calculations by Bender *et al.* [18] are also listed. The experimental data are those taken from  $B(E2)$  data in Ref. [36], and  $Q_0^t$  values determined by Doppler-shift analysis in Refs. [12] and [13]. <sup>a</sup>For the values of Refs. [12] and [13], a single  $Q_0^t$  value is assumed for the entire transitions in each of the “band 2” or the “band 1”.

$J_i$	AMD	GCM+HFBCS	shell model	Nucl. data. [36]	Ideguchi <i>et al.</i> [12]	Chiara <i>et al.</i> [13]
ND	(A2)				band 2	band 2
$2^+$	57	75.2		$1.1 \pm 0.1 \times 10^2$	$74 \pm 14^a$	
$4^+$	64	23.9		$1.3 \pm 0.2 \times 10^2$	$74 \pm 14^a$	
$6^+$	64	77.4			$74 \pm 14^a$	
$8^+$	78				$74 \pm 14^a$	
$10^+$	105				$74 \pm 14^a$	
$12^+$	112				$74 \pm 14^a$	
SD	(A3) ((A2))		8p-8h		band 1	band 1
$2^+$	129	133.9	172		$180 + 39 - 29^a$	$130 \pm 5^a$
$4^+$	129	97.6	170	$1.4 \pm 0.2 \times 10^2$	$180 + 39 - 29^a$	$130 \pm 5^a$
$6^+$	121	160.2	167		$180 + 39 - 29^a$	$130 \pm 5^a$
$8^+$	97(70)	157.9	162		$180 + 39 - 29^a$	$130 \pm 5^a$
$10^+$	81(105)	161.2	157		$180 + 39 - 29^a$	$130 \pm 5^a$
$12^+$	78(112)		160		$180 + 39 - 29^a$	$130 \pm 5^a$

odd orbits with angular parts related to  $Y_{3,\pm 3}$ . The property of a valence single-particle level of the four is shown in Fig. 11(c). The particle-hole nature is found also in the  $\alpha$ -cluster states  $\Phi_{\text{AMD}}(N_{\text{os}} = 66_\alpha^{(+)})$  and  $\Phi_{\text{AMD}}(N_{\text{os}} = 68_\alpha^{(+)})$  obtained by the interaction(ii). Namely, these states have a 4p-4h feature as four valence neutrons occupy *fp*-like orbits with 75% negative-parity component in the  $\Phi_{\text{AMD}}(N_{\text{os}} = 68_\alpha^{(+)})$  as seen in Fig. 11(f).

Thus, the single-particle levels in the intrinsic states disclose the many-particle many-hole characters in  $^{40}\text{Ca}$ . On the other hand, the cluster aspect has been found in prolate states which have parity-asymmetric shapes. It raises a question how the cluster aspect links with the mean-field aspect. Here we examine the cluster aspect while paying attention to parity asymmetry of the single-particle orbits. In Fig.12, we show the ratio of negative-parity component of the single-particle proton orbits in the prolate states  $\Phi_{\text{AMD}}(N_{\text{os}}^{(+)})$ . The behavior of the neutron orbits is almost the same as that of the proton orbits. At almost the spherical  $N_{\text{os}} = 62$  region, 12 protons( $\varphi_{a=1-12}^{\text{HF}}$ ) occupy almost parity-even orbits and 6 protons( $\varphi_{a=13-18}^{\text{HF}}$ ) are in almost parity-odd orbits, which indicates the approximately *sd*-shell closed configuration of this state. With the increase of  $N_{\text{os}}$ , the parity-odd components in the highest four levels( $\varphi_{a=1-4}^{\text{HF}}$ ) increase and these four levels become almost pure parity-odd orbits at  $N_{\text{os}} = 70$ . It means that four protons in the *sd*-shell are excited into the *fp*-shell. In the state  $\Phi_{\text{AMD}}(N_{\text{os}}^{(+)}) = 70^{(+)}$ , each of the higher ten levels  $\varphi_{a=1-10}^{\text{HF}}$  has approximately good parity. Instead, the parity symmetry breaking in single-particle orbits is rather remarkable in the 11th and 12th levels( $\varphi_{a=11,12}^{\text{HF}}$ ) which are originally the lowest *sd*-orbits as shown in Fig.12 (b). In order to see the effect of the single-particle features on the collective shape of the total system  $\Phi_{\text{AMD}}(N_{\text{os}}^{(+)}) = 70^{(+)}$ , we show the density distribution summed up for the protons in the lower levels( $\varphi_{a=11-20}^{\text{HF}}$ ) and that for the protons in the higher levels( $\varphi_{a=1-10}^{\text{HF}}$ ) in Fig.13. The most striking thing is that 10 protons in the lower levels form a parity asymmetric shape, which reminds us of the  $\alpha+^{16}\text{O}$  clustering in  $^{20}\text{Ne}$  system. These results imply that the parity asymmetry in this state dominantly originates not in the valence nucleons near the Fermi surface but in the  $\alpha$ -cluster-like correlation in the core part. It is inconsistent with an mean-field picture that nucleons at the surface may contribute such an exotic shape as the octupole deformation. We here remind the reader that this state( $\Phi_{\text{AMD}}(N_{\text{os}}^{(+)}) = 70^{(+)}$ ) is the dominant component of the superdeformation and has the  $^{12}\text{C}+^{28}\text{Si}$ -cluster structure(Fig.13(c)). The  $^{12}\text{C}+^{28}\text{Si}$  clustering is also seen in the aspect of molecular resonances. This seems to be inconsistent with possible  $^{32}\text{S}+2\alpha$  clustering, which may be naively expected from the 8p-8h nature of the superdeformed state. By the analysis of single-particle orbits, we can interpret the appearance of the  $^{12}\text{C}$  cluster as follows. The origin of the  $^{12}\text{C}$  cluster in the superdeformation is understood by the correlation within 12 nucleons; 4 *sd*-shell nucleons with the  $\alpha$  correlation and the 8 valence nucleons in the *fp*-like orbits. It leads to a new picture of the coexisting cluster and mean-field aspect. Namely, the deeply bound nucleons compose the parity-asymmetric core  $^{20}\text{Ne}$  with the  $\alpha$ -cluster correlation, while the single-

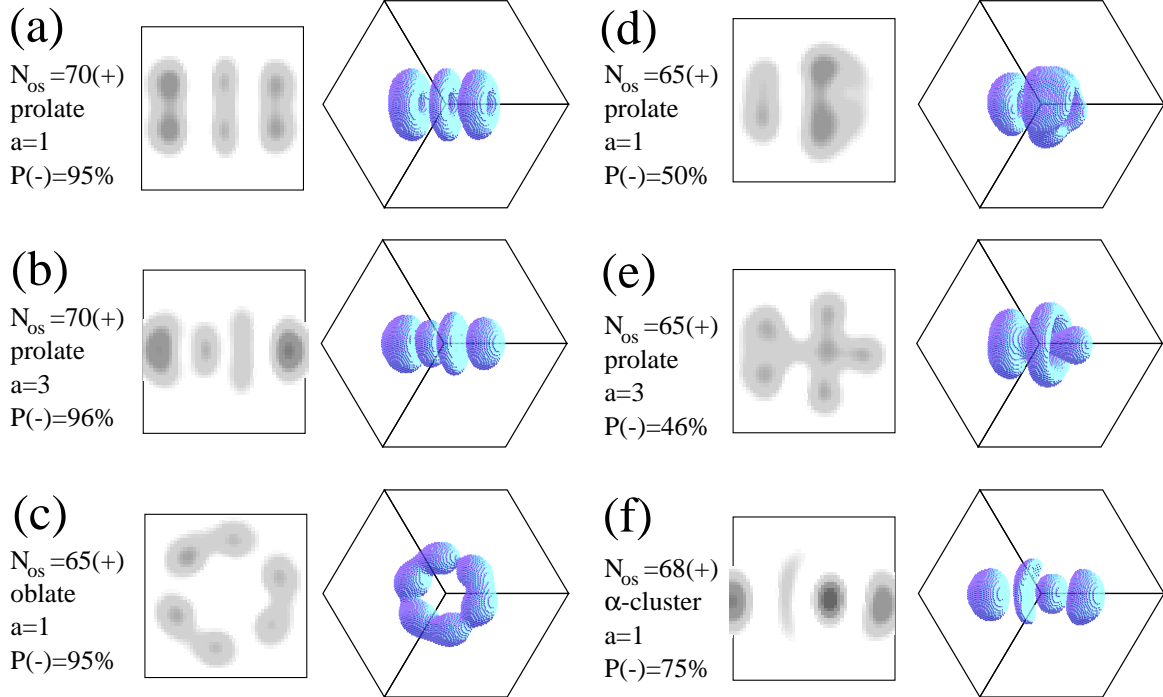


FIG. 11. (Color online) jDensity distributions of the HF-like single-particle orbits  $\varphi_a^{\text{HF}}$  for protons in  $\Phi_{\text{AMD}}(N_{\text{os}}^{(\pm)})$ . The results are for the calculations with the interaction(i) except for the panel(f). The first( $\varphi_{a=1}^{\text{HF}}$ ) and the third( $\varphi_{a=3}^{\text{HF}}$ ) highest proton orbits in the the dominant component( $\Phi_{\text{AMD}}(N_{\text{os}}^{(\pm)} = 70^{(+)})$ ) of the superdeformation are shown in (a) and (b), respectively. (c) The highest orbit,  $\varphi_{a=1}^{\text{HF}}$ , in the oblate solution with  $N_{\text{os}}^{(\pm)} = 65^{(+)}$ . (d)The first( $\varphi_{a=1}^{\text{HF}}$ ) and (e)the third( $\varphi_{a=3}^{\text{HF}}$ ) orbits in the prolate solutions with  $N_{\text{os}}^{(\pm)} = 65^{(+)}$ . (f) The highest( $\varphi_{a=1}^{\text{HF}}$ ) orbit in the  $\alpha$ -cluster state with  $N_{\text{os}}^{(\pm)} = 68^{(+)}$  obtained in the results with the interaction(ii). In the left side, the intrinsic state is projected onto the  $Y$ - $Z$  plane, and the density is integrated along the  $X$  axis, where  $X$ ,  $Y$  and  $Z$  axes are chosen as  $\langle X^2 \rangle \leq \langle Y^2 \rangle \leq \langle Z^2 \rangle$  and  $\langle XY \rangle = \langle YZ \rangle = \langle ZX \rangle = 0$ . The right figures are for the surface cut of the density. The percentage  $P(-)$  of the negative-parity component in each single-particle orbit is also listed. The box size is 10 fm.

particle levels at the energy surface have particle-hole nature. In the further large  $N_{\text{os}}$  region, the particle-hole nature disappears because of the spatial development of  $^{12}\text{C}+^{28}\text{Si}$  clustering.

## V. SUMMARY

We studied deformed states in  $^{40}\text{Ca}$  with antisymmetrized molecular dynamics(AMD) by using effective nuclear interactions which contain finite-range 2-body and 3-body forces. In the framework of a constraint AMD method, we performed parity projection before energy variation, and total-angular-momentum projection after the energy variation. The obtained AMD wave functions are superposed to get better wave functions.

By analyzing the calculated results of the intrinsic states, level scheme, and  $E2$  transition strengths, it was found that the rotational bands with various deformations appear in  $^{40}\text{Ca}$  as well as the spherical ground state. Namely, above the spherical ground state, the rotational bands arise from the normal-deformed state and the superdeformed state as well as the oblate state. In the results with a weaker spin-orbit force, we also obtained the  $\alpha$ -cluster-like bands. The present results of the superdeformed band reasonably reproduce the properties of the experimental superdeformed band build on the  $0_3^+(5.21 \text{ MeV})$ . On the other hand, we could not obtain a satisfactory description of the experimental deformed band build on the  $0_2^+(3.35 \text{ MeV})$ . Possible assignment of this band is to the theoretical normal-deformed band, the  $\alpha$ -cluster band, or admixture of them.

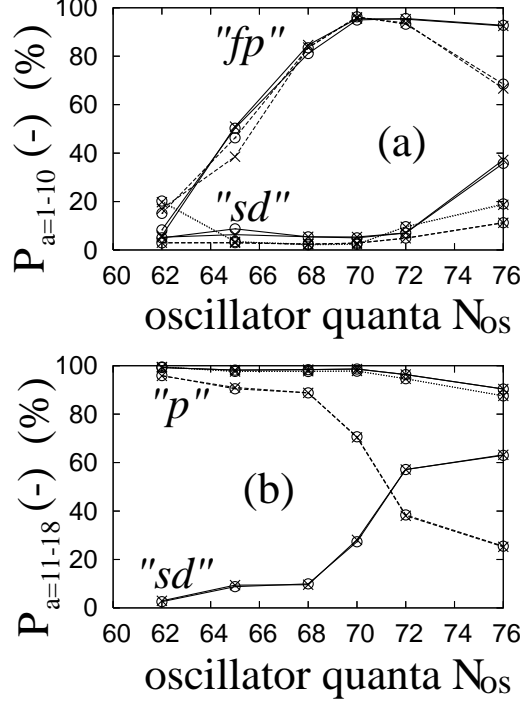


FIG. 12. The percentage  $P(-)$  of the negative-parity component in each HF-like single-particle orbit for the protons in the prolate states  $\Phi_{\text{AMD}}(N_{\text{os}}^{(+)})$  obtained with the interaction(i). The values  $P(-)$  for the highest ten levels( $a = 1 - 10$ ) are shown in the upper panel, and those for the orbits( $a = 11 - 18$ ) from the 11th to the 18th level are shown in the lower panel.

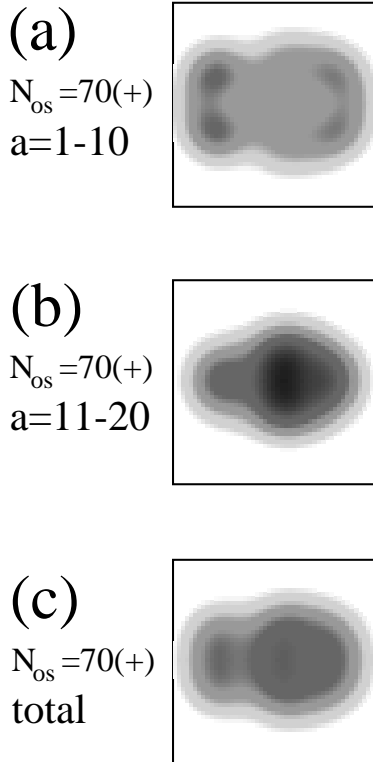


FIG. 13. Density distributions summed up (a) for the protons in the higher single-particle levels ( $\varphi_{a=1-10}^{\text{HF}}$ ) and (b) for the protons in the lower single-particle levels( $\varphi_{a=11-20}^{\text{HF}}$ ) in the intrinsic state of the superdeformation: $\Phi_{\text{AMD}}(N_{\text{os}} = 70^{(+)})$ . The total density is also shown in (c). The densities in (a) and (b) are normalized by a factor 4.

In the analysis of single-particle orbits, we found the particle-hole nature of the superdeformed state, the oblate state and the  $\alpha$ -cluster state, which are dominated by the  $8p-8h$ ,  $4p-4h$  and  $4p-4h$  configurations, respectively. On the other hand, the normal deformation in the present results contains mixing of  $2p-2h$ ,  $4p-4h$  and  $6p-6h$  configurations.

One of new findings in the present study is that the superdeformed state has a parity asymmetric shape with  $^{12}\text{C}+^{28}\text{Si}$ -like cluster structure. From the point of view of a single-particle picture, we discussed the relation between the cluster aspect and the many-particle many-hole aspect. We found that the origin of the  $^{12}\text{C}$  clustering in the superdeformed state is understood by the correlation of 12 nucleons; 4  $sd$ -shell nucleons with the  $\alpha$ -cluster correlation and the 8 valence nucleons in the  $fp$ -like orbits. It reveals the coexistence of cluster and mean-field aspect in the superdeformed state. Namely, the  $\alpha$ -cluster correlation in deeply bound nucleons composing the core  $^{20}\text{Ne}$  plays an important role in the parity asymmetric shape, while the particle-hole nature arises in the single-particle levels at the energy surface. The present result of the dominant  $8p-8h$  feature in the superdeformation seems to be consistent with the strong population of the members in the superdeformed band observed in 8-nucleon-transfer reactions;  $^{32}\text{S}(^{12}\text{C},\alpha)^{40}\text{Ca}$  [11]. However, it is inconsistent with the GCM+HFBCS calculations [18], where neither the  $4p-4h$  nor the  $8p-8h$  HF solutions can be assigned to the bandheads of the normal-deformed band or superdeformed band. One of the advantages of the present framework is the parity projection before energy variation, which is considered to be important in arising of the parity-asymmetric deformation. We think that one of the key properties which stabilize the “ $8p-8h$ ” character in the superdeformed band is the  $^{12}\text{C}+^{28}\text{Si}$  clustering which causes a parity asymmetric shape. Compared with the GCM+HFBCS calculations [18], the higher correlations are ignored in the present calculations. For example, the number of the basis in the superposition is ten at most, which is much smaller than the case of the GCM+HFBCS calculations [18]. Moreover, since we adopt the constraint on the total number of HO quanta in the energy variation, some basis are missed in terms of GCM with respect to the generator coordinate  $\beta_2$ , which are often used in the GCM+HF calculations. The pairing correlations are also ignored. It is an remaining problem to check how the properties of the superdeformation are affected by introducing these effects.

Above the superdeformed band, we found possible higher rotational bands based on  $^{12}\text{C}+^{28}\text{Si}$ -clustering in the large prolate deformations. It is predicted that  $^{12}\text{C}+^{28}\text{Si}$  molecular bands may be built due to the excitation of the inter-cluster motion. The present results suggest that the superdeformed band and these higher molecular bands are regarded as a series of  $^{12}\text{C}+^{28}\text{Si}$  molecular bands. This means that the  $^{12}\text{C}+^{28}\text{Si}$  cluster aspect is rather prominent in the superdeformed state than  $^{32}\text{S}+2\alpha$  aspect, although the latter may be naively expected from the  $8p-8h$  feature of this state. We also suggest the negative-parity bands caused by the parity asymmetric deformation.

In the present work, we use the stronger spin-orbit force than the nuclear interaction adopted in Ref. [30] to quantitatively reproduce the excitation energies of the superdeformed band and negative parity states. With the original weak spin-orbit force, the excitation energies of all the excited states in  $^{40}\text{Ca}$  are overestimated. We would like to stress again that the intra-band properties such as energy spectra,  $E2$  transitions and intrinsic structure of the superdeformed band are not sensitive to choice of either interaction. In order to solve the remaining problems, it may be necessary to introduce a suitable nuclear interaction and extended model wave functions.

## ACKNOWLEDGMENTS

The authors would like to thank Prof. H. Horiuchi and Dr. Taniguchi for many discussions. They are also thankful to Dr. Ideguchi and Dr. Inakura for valuable comments. The computational calculations in this work were supported by the Supercomputer Projects of High Energy Accelerator Research Organization(KEK). This work was supported by Japan Society for the Promotion of Science and a Grant-in-Aid for Scientific Research of the Japan Ministry of Education, Science and Culture. A part of the work was performed in the “Research Project for Study of Unstable Nuclei from Nuclear Cluster Aspects” sponsored by Institute of Physical and Chemical Research (RIKEN).

## REFERENCES

---

- [1] J. R. Macdonald, D. H. Wilkinson and D. E. Alburger, Phys. Rev. C **3**, 219 (1971), and references therein.
- [2] W. J. Gerace and A. M. Green, Nucl. Phys. **A93**, 110 (1967).
- [3] W. J. Gerace and A. M. Green, Nucl. Phys. **A123**, 241 (1969).

[4] R. R. Betts, H. T. Fortune, J. N. Bishop, M. N. I. Al-Jadir and R. Middleton, Nucl. Phys. **A292**, 281(1977).

[5] H. T. Fortune, M. N. I. Al-Jadir, R. R. Betts, J. N. Bishop and R. Middleton, Phys. Rev. C **19**, 756 (1979).

[6] T. Yamaya *et al.*, Nucl. Phys. **A573**, 154(1994).

[7] T. Yamaya, K. Katori, M. Fujiwara, S. Kato and S. Ohkubo, Prog. Theor. Phys. Suppl. **132**, 73 (1998).

[8] S. Ohkubo and K. Umehara, Prog. Theor. Phys. **80**, 598 (1988).

[9] T. Sakuda and S. Ohkubo, Phys. Rev. C **49**, 149 (1994).

[10] T. Sakuda and S. Ohkubo, Prog. Theor. Phys. Suppl. **132**, 103 (1994).

[11] R. Middleton, J. D. Garrett and H. T. Fortune, Phys. Lett. **39B**, 339 (1972).

[12] E. Ideguchi *et al.*, Phys. Rev. Lett. **87**, 222501 (2001)

[13] C. J. Chiara *et al.*, Phys. Rev. C **67**, 041303(R) (2003).

[14] D. C. Zheng, D. Berdichevsky and L. Zamick, Phys. Rev. C **38**, 437 (1988).

[15] D. C. Zheng, L. Zamick and D. Berdichevsky, Phys. Rev. C **42**, 1004 (1990).

[16] T. Inakura, S. Mizutori, M. Yamagami and K. Matsuyanagi, Nucl. Phys. **A 710**, 261 (2002).

[17] G. Leander and S. E. Larsson, Nucl. Phys. **A239**, 93 (1975).

[18] M. Bender, H. Flocard and P. -H. Heenen, Phys. Rev. C **68**, 044321 (2003).

[19] A. Poves, E. Caurier, F. Nowacki and A. Zuker, Eur. Phys. J. A **20**, 119(2004)

[20] Y. Kanada-En'yo, M. Kimura and H. Horiuchi, Comptes rendus Physique Vol.4, 497 (2003).

[21] M. Kimura, Phys. Rev. C **69**, 044319 (2004).

[22] M. Kimura and H. Horiuchi, Phys. Rev. C **69**, 051304(R) (2004).

[23] R. A. Racca, P. A. Deyoung, J. J. Kolata and R. J. Thornburg, Phys. Lett. **129B**, 294 (1983).

[24] R. Ost *et al.*, Phys. Rev. C **19**, 740 (1979).

[25] Y. Kanada-En'yo and H. Horiuchi, Prog. Theor. Phys. **93**, 115 (1995).

[26] M. Kimura, Y. Sugawa and H. Horiuchi, Prog. Theor. Phys. **106**, 115 (2001).

[27] M. Kimura, H. Horiuchi, Prog. Theor. Phys. **107**, 33 (2002).

[28] Y. Kanada-En'yo, Phys. Rev. C **71**, 014303 (2005).

[29] Y. Taniguchi, M. Kimura and H. Horiuchi, Prog. Theor. Phys. **112**, 475 (2004).

[30] Y. Kanada-En'yo and Y. Akaishi, Phys. Rev. C **69**, 034306 (2004).

[31] Y. Kanada-En'yo, H. Horiuchi and A. Ono, Phys. Rev. C **52**, 628 (1995); Y. Kanada-En'yo and H. Horiuchi, Phys. Rev. C **52**, 647 (1995).

[32] Y. Kanada-En'yo and H. Horiuchi, Prog. Theor. Phys. Suppl. **142**, 205 (2001).

[33] S. Marcos, H. Flocard, and P. H. Heenen, Nucl. Phys. **A 410**, 125 (1983).

[34] N. Yamaguchi, T. Kasahara, S. Nagata and Y. Akaishi, Prog. Theor. Phys. **62**, 1018 (1979); R. Tamagaki, Prog. Theor. Phys. **39**, 91 (1968).

[35] A. Bohr and B. R. Mottelson, *Nuclear Structure Vol. II*, (W. A. Benjamin, New York, 1975).

[36] At. Data Nucl. Data Tables **23**, 3 (1979).

[37] J. L. Wood *et al.*, Phys. Rep. **215**, 101 (1992).

[38] P. Braun-Muzinger and J. Barrette, Phys. Rep. **87**, 209 (1982).

[39] W. Greiner, J. Y. Park and W. Scheid, "Nuclear MOlecules", (World Scientific, Singapore, 1995).

[40] D. Baye and P.-H. Heenen, Nucl. Phys. **A283**, 176 (1977).

[41] K. Kato, S. Okabe and Y. Abe, Prog. Theor. Phys. **74**, 1053 (1985).

[42] Y. Kanada-En'yo, *Proc. of Frontiers of Collective Motions(CM2002)*, Aizu, Japan(2002), ed. by H. Sagawa and H. Iwasaki, 254.

[43] A. Dóte, H. Horiuchi and Y. Kanada-Enyo, Phys. Rev. C **56**, 1844 (1997).